

# Lattice-Boltzmann hydrodynamics of single-square-grid generated turbulence - a partial entropic stabilisation approach

Chin Vern Yeoh<sup>\*</sup>, Ean Hin Ooi, Ji Jinn Foo<sup>\*</sup>

School of Engineering, Monash University Malaysia, 47500 Bandar Sunway, Selangor, Malaysia



## ARTICLE INFO

### Article history:

Received 11 February 2020

Received in revised form 12 June 2020

Accepted 23 June 2020

Available online 2 July 2020

### Keywords:

Lattice-Boltzmann method

Partial entropic stabilisation

Large-eddy simulation

Turbulence

Space-filling grid

Single square grid

## ABSTRACT

Under-resolved direct numerical simulations of turbulence in the wake of a single-square-grid (SSG) are conducted using the lattice-Boltzmann method (LBM), with varying degrees of partial moment entropic stabilisation. Turbulence statistics along the grid centreline show satisfactory agreement with literature, greatly outperforming a control study employing the single-relaxation-time Smagorinsky LES model with equivalent resolution. The coarse-resolution entropic LBM simulations are able to capture the qualitative behaviour of the anisotropic and non-homogeneous turbulence generated by the SSG, indicating possible extension of the capability of the entropic lattice-Boltzmann method to simulate more exotic forms of turbulence beyond those reported by the majority of current studies. However, in the extreme near field of the single-square-grid, pseudo-compressibility effects, even at a low lattice Mach number, undermine LBM predictions for turbulence which is generated by action of the pressure Hessian — this is found to be an issue for all models studied, and not a numerical artefact of the entropic stabilisation. With regard to the action of the entropic stabiliser, a comparison of models employing differing degrees of stabilisation on higher-order natural moments suggest that the trace of the stress tensor should not be subject to entropic control for better accuracy in turbulence prediction.

© 2020 Elsevier Ltd. All rights reserved.

## 1. Introduction

### 1.1. Entropic stabilisation of the lattice-Boltzmann method for high-Reynolds number flow

The lattice-Boltzmann method (LBM) has gained much popularity in the previous two decades as a viable numerical tool for simulating a wide range of phenomena, ranging from particle suspensions [1] to fluid acoustics [2] to multiphase flows [3,4]. Moreover, as the nonlinear and nonlocal terms of the LBM are strictly separated, this allows the algorithm to be almost fully parallelisable, promising an efficiency minimally comparable to, if not exceeding, traditional Navier–Stokes solvers for hydrodynamic simulations [5]. However, a ubiquitous drawback of the LBM has been, and still is, its susceptibility to instabilities at very small relaxation times.

Hence, the development of more advanced and more stable collision models has proceeded together with the application of the LBM for ever-higher Reynolds numbers. Almost immediately after the initial LBM was formally proposed,

<sup>\*</sup> Corresponding authors.

E-mail addresses: [Chin.Yeoh@monash.edu](mailto:Chin.Yeoh@monash.edu) (C.V. Yeoh), [Foo.Ji.Jinn@monash.edu](mailto:Foo.Ji.Jinn@monash.edu) (J.J. Foo).

## Nomenclature

### Abbreviations

DNS	Direct numerical simulation
HIT	Homogeneous, isotropic turbulence
KBC-Nx	Karlin–Bosch–Chikatamarla collision model (N1–N4 natural moment basis)
LBM; ELBM	Lattice-Boltzmann method; (entropic) lattice-Boltzmann method
LES	Large-eddy simulation
MRT	Multiple-relaxation time (collision model)
RANS	Reynolds-averaged Navier–Stokes (equations)
SFG	Square-fractal grid
SGS	Subgrid-scales (modelling)
SRT	Single-relaxation time
SRT-LBGK	Single-relaxation time lattice Bhatnagar–Gross–Krook (collision model)
SSG	Single-square grid
NRMSE	Normalised root-mean-square error

### General Constants

$C$	Smagorinsky constant
$Ma$	Mach number
$Re$	Reynolds number
$\nu$	Kinematic viscosity (dimensionless)

### Lattice-Boltzmann Method

$c_s$	Lattice speed of sound (dimensionless)
$DnQm$	Lattice stencil in $n$ dimensions with $m$ discrete lattice velocities
$\vec{e}_\alpha$	$\alpha$ th Element of the discretised set of lattice velocity vectors
$f_\alpha$	Particle distribution function (also termed particle populations)
$F_\alpha$	Body force term (dimensionless)
$f_\alpha^{eq}$	Equilibrium particle distribution function
$f_\alpha^{mirr}$	Isentropic mirror-point particle distribution function
$h_\alpha, h_\alpha^{eq}$	Higher-order component of particle populations/equilibrium particle populations
$k_\alpha$	Kinematic component of particle populations
$M_{pqr}$	General expression for lattice moments
$N_{xz}, N_{yz}$	Normal stress differences
$S$	Strain-rate tensor for Smagorinsky LES modelling
$s_\alpha, s_\alpha^{eq}$	Shear component of particle populations/equilibrium particle populations
$T$	Trace of the stress tensor
$\vec{u}$	Macroscopic velocity in Cartesian coordinate system (dimensionless)
$w_\alpha$	Lattice weights
$\alpha$	$\alpha$ th Element of the discretised set of lattice velocities
$\beta$	Collision relaxation parameter
$\gamma$	Entropic stabilisation parameter
$\Delta_x$	Subgrid-scale dimension (LES)
$\nu_t$	Local eddy viscosity (dimensionless)
$\Pi_{xy}, \Pi_{yz}, \Pi_{xz}$	Off-diagonal stress tensor components
$\rho$	Macroscopic fluid density (dimensionless)
$\tau$	Relaxation time parameter for SRT (dimensionless)
$\tau_{eff}$	Effective relaxation time parameter for SRT-LES (dimensionless)
$\varphi_i$	Lattice acceleration for simple body forcing (dimensionless)
$\Omega_\alpha$	Collision operator

### Turbulence and Velocity-Gradient Tensor Variables

$C_k$	Convection by mean flow term (turbulence kinetic energy budget)
-------	---

$C_s$	Convection by mean flow term (mean strain-rate product budget)
$D_k$	Viscous diffusion term (turbulence kinetic energy budget)
$F_{u_x}$	Streamwise velocity fluctuation flatness
$L_0$	Bar length of first grid iteration
$P_k$	Production by mean flow term (turbulence kinetic energy budget)
$P_s$	Strain self-amplification term (mean strain-rate product budget)
$R_{xx}$	Streamwise velocity fluctuation autocorrelation vector
$S_{u_x}$	Streamwise velocity fluctuation skewness
$S_{ij}$	Mean velocity strain-rate tensor
$s_{ij}$	Velocity fluctuation strain-rate tensor
$t_0$	Bar thickness of first grid iteration
$T_k$	Transport by turbulent fluctuations term (turbulence kinetic energy budget)
$T_s$	Transport by turbulent fluctuations term (mean strain-rate product budget)
$TI$	Turbulence intensity
$TKE$	Turbulence kinetic energy
$U_\infty$	Freestream velocity
$U$	Flow mean velocity
$u_x$	Velocity fluctuations in the streamwise direction
$u'_x$	Nondimensionalised velocity fluctuation
$u_x^*$	Instantaneous velocity in the streamwise direction
$x$	Cartesian coordinate aligned with the streamwise direction
$x^*$	Wake-interaction length scale (in the context of grid-generated turbulence)
$y, z$	Cartesian coordinates aligned with the lateral directions
$\Gamma_t$	Turbulent intermittency
$\Delta/\eta$	Ratio of mesh (lattice cell) size to local estimated Kolmogorov length scale
$\epsilon_k$	Viscous dissipation term (turbulence kinetic energy budget)
$\pi_k$	Pressure work term (turbulence kinetic energy budget)
$\pi_s$	Pressure Hessian term (mean strain-rate product budget)
$\sigma_{SSG}$	Blockage ratio for single-square grid
$\phi$	Simulation-predicted turbulence statistic (first- to- fourth order)
$\hat{\phi}$	Experiment-measured turbulence statistic (first- to- fourth order)
$\omega_i$	Fluctuation vorticity vector
$ \omega ,  \omega _{th}$	Magnitude of fluctuation vorticity vector; threshold value of vorticity magnitude

employing the single-relaxation time (SRT-LBGK) collision model [6,7], d’Humières [8] formulated the multiple-relaxation-time (MRT) collision model that allowed for independent relaxation of moments — this has since been refined to the cascaded [9] and most recently, the cumulant [10] models, with a key benefit being improved stability over the BGK model. However, a careful search of the relaxation parameter space for an optimal set of values must be done [11–13] — this quickly becomes tedious for larger stencils such as the D3Q19 and D3Q27 lattices, with many ‘free’ parameters. Nonetheless, the MRT model is currently the workhorse for many LBM studies.

Following a (up to recently) separate branch of development, Karlin et al. proposed stabilising the LBM collision using entropic principles via a discrete  $H$ -theorem [14,15], kickstarting the class of entropic lattice-Boltzmann models (ELBMs). This provided a more physical interpretation of ensuring non-negativity of over-relaxed particle populations beyond a simple positive-enforcing numerical limiter [16], assuring that the post-collisional state maintained the entropy of the local collision and did not reduce it [17]. A significant advantage of the ELBM was the raising of the attainable Reynolds number to considerably larger values, even with severely non-scale-resolving coarse meshes [18,19]. Earlier formulations of the ELBM were limited to the SRT collisional model by adjusting the effective relaxation time; however, this had the drawbacks of a non-constant shear viscosity which affected the local hydrodynamics, as well as the requirement of an implicit solution for the entropic stabiliser [20].

The most recent formulation of the ELBM, termed by its proponents as the KBC model [21,22], holds promise of combining the strengths of the traditional MRT and the SRT-ELBM collision models by limiting the extent of entropic stabilisation to moments of second order and higher. This leaves the deviatoric stress tensor unmodified, while keeping the higher-order moments under entropic control; furthermore, the KBC model is fully explicit, recovering a certain amount of computational efficiency. Hence, one may interpret the KBC-ELBM model as an explicit MRT model with an algebraic formulation for a subset of its higher-order relaxation parameters, [19], viz, an entropic multirelaxation time LBM. At the

moment, the KBC-ELBM model is slowly gaining use for a range of studies [19,23–25], but has yet to see widespread adoption.

The underlying physics of the ELBM, translated from the microscale collision model to its effect on macroscale flow behaviour, is also a topic warranting further study, given its bearing on subgrid-scale (SGS) turbulence modelling for unresolved flow dynamics. This was most prominently discussed by Malaspinas et al. [26] who derived a subgrid model of the SRT-ELBM via the Chapman–Enskog expansion. On the other hand, a direct expansion of this to the entropic multirelaxation LBM algorithm is not trivial. However, the influence of entropic stabilisation on higher-order moments is certain to have an effect on the evolution of turbulent behaviour, as indicated in a recent parallel study by Gehrke et al. [27]. The effect of this partial stabilisation on the flow dynamics remains an open question, especially for exotic turbulence cases beyond current benchmark problems.

### 1.2. Past lattice-Boltzmann DNS and LES studies of turbulence

With its promise of significant gains in computational efficiency via massive parallelisation, the LBM has been employed in numerous fully-resolved direct numerical simulation (DNS) studies since its inception [28,29]. Such simulations were limited to relatively low turbulent Reynolds numbers, but their excellent agreement with literature cemented the LBM as a capable alternative for scale-resolving flow simulations. Recent LBM-DNS studies of note include those by Nathen et al. [5] and Peng et al. [30] for plane and pipe turbulent channel flow.

Concurrent to such LBM-DNS studies are the LBM-large-eddy simulation (LBM-LES) studies, where SGS models [31,32] are directly incorporated into the LBM collision step by adjusting the relaxation time based on local strain rate. This is a favourable compromise between efficiency, stability, and accuracy, preserving the locality of the algorithm while enhancing stability by reducing the possibility of over-relaxation to negative regions. The LBM-LES algorithm has been also applied to various turbulence case studies, including decaying HIT [33] and flow past cylinders [34]. In the context of the present study, however, it is worth noting that the only LBM study on grid turbulence as documented in the literature is the SRT-LES study performed by Djendi [35].

With regard to the employment of the entropic lattice-Boltzmann method in turbulent flows, previous test cases include decaying HIT [22,36], dipole–dipole interaction [26], turbulent channel flows [18], magnetohydrodynamics [19], and, flow around aerofoils and surface-mounted cylinders [23,37]. This reiterates the need to employ the test case of grid-wake turbulence to further explore the capabilities (and limitations) of both the entropic algorithm, as well as the LBM in general.

### 1.3. Turbulence behind the single-square-grid

While grid-generated turbulence has been a mainstay of freely evolving turbulence studies [38,39], it was not until recently that attention was drawn to the evolution of grid turbulence in the relative near field, and for ‘space-filling’ grid cases; i.e. where the grid mesh length is of comparable dimension to the tunnel height. Following the seminal work of Hurst and Vassilicos [40], there has been a resurgence of interest in turbulence generated by ‘fractal grids’, with square fractal grids (SFGs) being the most prominent geometry. Due to their reported ability to generate energetic multiscale turbulent fluctuations in the near field [41,42], along with an extended production region with intense shedding events [43], SFGs have quickly found their way into engineering applications where passive control of turbulence is desirable, e.g. heat transfer for impinging jets [44], walls [45], cylinders [46], and finned heat sinks [47].

However, the full mechanisms of multiscale interactions in SFG-generated turbulence are not completely understood. This led to a series of foundational DNS studies by Zhou et al. where the grid geometry was scaled into a one-iteration single-square-grid (SSG) [48–50]. By claiming the SSG as a fundamental building block for both regular and square fractal grids, they were able to isolate and quantify the evolution of turbulence generation and decay downstream of the SSG. This was further supplemented by a combined experimental/DNS work by Laizet et al. [51] which provided experimental data as a reference for turbulence evolution along the SSG centreline. Finally, in a high-resolution DNS study by Paul et al. [52], the full picture of turbulence evolution along the SSG centreline was quantified by an exhaustive study into the dynamics of the velocity-gradient-tensor.

Nonetheless, current computational studies of both SFG- and SSG-generated turbulence have insofar been constrained to traditional Navier–Stokes high-performance DNS (and limited LES [53]) studies in order to promise high accuracy for turbulent fluctuation predictions, as well as higher-order statistics – these cannot be neglected due to their influence on intermittent, intense events that contribute greatly to improving turbulent transport [52,54]. Hence, the motivation of employing the LBM to model such grid-generated turbulence can be seen as twofold: firstly, to investigate the capabilities of the LBM and entropic algorithms in modelling exotic turbulent applications, and secondly, to establish the feasibility of the method as a lower-cost alternative to DNS studies for said turbulence. The present work seeks to employ the entropic multirelaxation LBM (with the SRT-Smagorinsky model as a control comparison) in the form of an under-resolved DNS to model the turbulent field along the centreline behind a single-square-grid. With the recent additions to literature by Laizet et al. [51] and Paul et al. [52], these are used as benchmarks to validate and contrast the turbulence statistics, along with the physical mechanisms of turbulence generation behind the SSG by an investigation of velocity-gradient-tensor dynamics and the associated budgets. Finally, the effect of the extent of entropic stabilisation are also investigated by

**Table 1**  
Linkage and weighting parameters for the present D3Q27 LBM stencil.

Stencil	$\alpha$	$ \vec{e}_\alpha $	$\vec{e}_\alpha$	$w_\alpha$
D3Q27	1	0	(0, 0, 0)	8/27
	2, ..., 7	1	( $\pm 1, 0, 0$ ), ( $0, \pm 1, 0$ ), ( $0, 0, \pm 1$ )	2/27
	8, ..., 19	$\sqrt{2}$	( $\pm 1, \pm 1, 0$ ), ( $0, \pm 1, \pm 1$ ), ( $\pm 1, 0, \pm 1$ )	1/54
	20, ..., 27	$\sqrt{3}$	( $\pm 1, \pm 1, \pm 1$ )	1/216

comparing the turbulent fields generated by the KBC-N1 to KBC-N4 models [22] in order to identify the influence of higher-order moments on the turbulence statistics.

This paper is organised as follows: Section 2 documents the numerical method and setup of the study, where the theoretical details of the LBM and the associated collision/LES models are given in Section 2.1. Section 2.2 presents the computational domain and boundary conditions; in particular, a novel method of approximating an open outflow boundary condition is given in Section 2.2.3. Data gathering details are briefly summarised in Section 2.3. Moving on, Sections 3 and 4 and present the validation and comparison of the KBC-N4 and SRT-Smagorinsky models with literature and DNS values in terms of one-point statistics (Sections 3.1 and 4.1), the turbulence kinetic energy budgets (Sections 3.2 and 4.2), and spectra (Section 3.5). Further investigation into the behaviour of the LBM models and the entropic stabiliser are given in Sections 3.3, 3.4, and 4.3. Finally, a comparison between the KBC-N1 to KBC-N4 models is presented in Section 5, and the employability of the models with larger degrees of entropic stabilisation is briefly discussed.

## 2. Computational setup and methodology

### 2.1. Lattice-Boltzmann method

#### 2.1.1. General outline

In classical form, the LBM involves solving the spatial- and temporal-discretised Boltzmann equation for discrete particle populations via a two-step streaming and collision procedure, summarised by Eq. (1):

$$f_\alpha(\vec{x} + \vec{e}_\alpha \delta_t, t + \delta_t) = f_\alpha(\vec{x}, t) + \Omega_\alpha \quad (1)$$

where  $f_\alpha(\vec{x}, t)$  is the particle distribution function at position  $\vec{x}$  and time  $t$ ,  $\Omega_\alpha$  the collision operator which accounts for the local change in particle distribution due to collision and scattering interactions, and  $\delta_t$  the lattice time step. The subscript  $\alpha$  denotes the  $\alpha$ th element of the discretised set of lattice velocities, and the associated lattice velocity vector  $\vec{e}_\alpha$  indicates the streaming direction. For vector/tensor notation in this paper, Greek subscripts indicate a basis following the lattice stencil, while Roman subscripts or the right-arrow accent indicate a basis following the Cartesian coordinate system, and both conventions are used interchangeably.

Commonly,  $\delta_t$  is set to 1, and the components of  $\vec{e}_\alpha$  given as  $e_{\alpha i} \in \{-1, 0, 1\}$ . This results in an effective lattice sound speed  $c_s = c/\sqrt{3} = 1/\sqrt{3}$ . For this study, the D3Q27 stencil is employed to reduce errors arising from insufficient isotropy and frame invariance, as documented in previous studies [13,30,55]. The above results in the lattice scheme reported in Table 1, where the associated weights  $w_\alpha$  are given as,

$$w_\alpha = w_{e_{\alpha x}} w_{e_{\alpha y}} w_{e_{\alpha z}}, \alpha \in \{1, 2, \dots, 27\} \quad (2)$$

and by Gauss–Hermite quadrature,

$$w_0 = \frac{2}{3}, w_{-1} = w_1 = \frac{1}{6}. \quad (3)$$

To obtain the macroscopic variables of fluid density  $\rho$  and velocity  $u_i$ , the zeroth- and first-order discrete moments are employed such that,

$$\rho(\vec{x}, t) = \sum_{\alpha=1}^{27} f_\alpha(\vec{x}, t) \quad (4)$$

$$\rho \vec{u}(\vec{x}, t) = \sum_{\alpha=1}^{27} \vec{e}_\alpha f_\alpha(\vec{x}, t) \quad (5)$$

Collision in the LBM entails relaxing populations to an equilibrium value  $f_\alpha^{eq}$ , or, in moment space,  $m_\alpha^{eq}$ , given as a linear combination of  $f_\alpha^{eq}$ . While the most common method of computing  $f_\alpha^{eq}$  is via the second order-truncated polynomial expansion; here, we choose to follow Karlin et al.'s 'exact equilibrium' [14] in order to isolate completely the effects of the entropic operator on fluid flow behaviour [21,22]:

$$f_\alpha^{eq} = w_\alpha \rho \Psi [B(u_x)]^{e_{\alpha x}} [B(u_y)]^{e_{\alpha y}} [B(u_z)]^{e_{\alpha z}} \quad (6)$$

with subfunctions  $\Psi(A)$ ,  $A$ , and  $B$  defined respectively as

$$\Psi(A) = A(u_x)A(u_y)A(u_z) \quad (7)$$

and

$$A(x) = 2 - \sqrt{1 + 3x^2} \quad (8)$$

$$B(x) = \frac{2x + \sqrt{1 + 3x^2}}{1 - x} \quad (9)$$

Finally, for a section of the computational domain (further details in Section 2.2.3), ‘simple forcing’ [56] is employed such that an additional term is added in the LBM post-collisional state:

$$f_\alpha(\vec{x} + \vec{e}_\alpha \delta_t, t + \delta_t) = f_\alpha(\vec{x}, t) + \Omega_\alpha + F_\alpha(\vec{x}, t) \quad (10)$$

with  $F_\alpha$  given as,

$$F_\alpha = w_\alpha \rho \frac{e_{\alpha i} \varphi_i}{c_s^2} \delta_t \quad (11)$$

where  $\varphi_i(\vec{x}, t)$  is the modelled acceleration due to external body forces. Note that while more accurate methods of including a body force are available [57], the portion of the computational domain employing the above does not overlap with the section where turbulence is studied.

The final component of the algorithm entails the collision step. In this study, the KBC-ELBM is employed along with the SRT model with Smagorinsky LES subgrid-scale modelling as a control, and both are discussed below. SGS modelling is applied for the SRT case as the unmodified SRT-LBGK model fails to converge (becomes unstable) at the current coarse mesh resolution.

### 2.1.2. The KBC model

In the context of ELBMs, the collision step entails a relaxation of the local population to a state of higher entropy via the following [21,36]:

$$f_\alpha^*(\vec{x}, t) = (1 - \beta)f_\alpha(\vec{x}, t) + \beta f_\alpha^{mirr}(\vec{x}, t) \quad (12)$$

with  $f_\alpha^*$  denoting the post-collisional state before advection,  $f_\alpha^{mirr}$  the isentropic ‘mirror point’ [17], and  $\beta$  the relaxation parameter associated with shear viscosity,  $\nu$  in the context of hydrodynamic transport. Upon a Chapman–Enskog analysis:

$$\nu = c_s^2 \left( \frac{1}{2\beta} - \frac{1}{2} \right) \quad (13)$$

In contrast to the SRT-LBGK model, which directly assumes

$$f_\alpha^{mirr} = 2f_\alpha^{eq} - f_\alpha \quad (14)$$

conservation of entropy requires  $f_\alpha^{mirr}$  to be a function of  $f_\alpha^{eq}$  and the entropic parameter  $\gamma(\vec{x}, t)$ , where  $\gamma$  (also known as the entropic stabiliser) is the maximiser of the entropy of the post-collisional state. Karlin et al. isolate the effect of  $\gamma$  by decomposing  $f_\alpha^{mirr}$  into the following moment representation:

$$f_\alpha^{mirr} = k_\alpha + [2s_\alpha^{eq} - s_\alpha] + [\gamma h_\alpha^{eq} - (\gamma - 1)h_\alpha] \quad (15)$$

with recovery of the SRT-LBGK model when  $\gamma = 2$ .

Here,  $k_\alpha$ ,  $s_\alpha$ , and  $h_\alpha$  are given as the ‘kinematic’, ‘shear’, and ‘higher-order’ parts of the particle populations, such that  $f_\alpha = k_\alpha + s_\alpha + h_\alpha$  (the same holds for the equilibrium populations), and are linear combinations of the lattice moments given by the general formula,

$$\rho M_{pqr} = \sum_{\alpha=1}^{27} f_\alpha e_{\alpha x}^p e_{\alpha y}^q e_{\alpha z}^r \quad (16)$$

For the scope of this study, only the natural moments are considered, corresponding to the KBC N1–N4 models. A summary of the moments associated with the stress tensor, and their associated abbreviations, are as follows (at unit density):

Trace of the stress tensor,

$$T = M_{200} + M_{020} + M_{002} \quad (17)$$

Normal stress differences,

$$N_{xz} = M_{200} - M_{002}, \quad N_{yz} = M_{020} - M_{002} \quad (18)$$

**Table 2**

Moment categorisation into the kinematic, shear, and optional-shear components for the KBC models in the natural basis.

$\vec{e}_\alpha$	$f$	$k$	$s$	$s^*$	$s^*$ - Inclusive models
(0, 0, 0)	$f_{(0,0,0)}$	$\rho$	0	$-\rho T$	KBC-N2, N4
( $\pm 1$ , 0, 0)	$f_{(e_x, 0, 0)}$	$\frac{1}{2}\rho e_x u_x$	$\frac{1}{6}\rho [2N_{xz} - N_{yz}]$	$\frac{1}{6}\rho T$	KBC-N2, N4
				$-\frac{1}{2}\rho e_x (M_{120} + M_{102})$	KBC-N3, N4
(0, $\pm 1$ , 0)	$f_{(0, e_y, 0)}$	$\frac{1}{2}\rho e_y u_y$	$\frac{1}{6}\rho [-N_{xz} + 2N_{yz}]$	$\frac{1}{6}\rho T$	KBC-N2, N4
				$-\frac{1}{2}\rho e_y (M_{210} + M_{012})$	KBC-N3, N4
(0, 0, $\pm 1$ )	$f_{(0, 0, e_z)}$	$\frac{1}{2}\rho e_z u_z$	$\frac{1}{6}\rho [-N_{xz} - N_{yz}]$	$\frac{1}{6}\rho T$	KBC-N2, N4
				$-\frac{1}{2}\rho e_z (M_{201} + M_{021})$	KBC-N3, N4
( $\pm 1$ , $\pm 1$ , 0)	$f_{(e_x, e_y, 0)}$	0	$\frac{1}{4}\rho e_x e_y \Pi_{xy}$	$\frac{1}{4}\rho (e_x M_{120} + e_y M_{210})$	KBC-N3, N4
(0, $\pm 1$ , $\pm 1$ )	$f_{(0, e_y, e_z)}$		$\frac{1}{4}\rho e_y e_z \Pi_{yz}$	$\frac{1}{4}\rho (e_y M_{012} + e_z M_{021})$	KBC-N3, N4
( $\pm 1$ , 0, $\pm 1$ )	$f_{(e_x, 0, e_z)}$		$\frac{1}{4}\rho e_x e_z \Pi_{xz}$	$\frac{1}{4}\rho (e_x M_{102} + e_z M_{201})$	KBC-N3, N4
( $\pm 1$ , $\pm 1$ , $\pm 1$ )	$f_{(e_x, e_y, e_z)}$		0	$\frac{1}{8}\rho e_x e_y e_z M_{111}$	KBC-N3, N4

and the off-diagonal stress tensor components,

$$\Pi_{xy} = M_{110}, \quad \Pi_{xz} = M_{101}, \quad \Pi_{yz} = M_{011} \quad (19)$$

Reverse-transforming the moments and categorising based on  $k_\alpha$  and  $s_\alpha$  leads to the list of population representations in Table 2, where  $s_\alpha^*$  denotes moments which may or may not be included in the shear category depending on which KBC-Nx model is used. A similar process may be done for the equilibrium populations and moments.

Finally, in order to complete the execution of Eq. (12), the calculation of the entropic parameter  $\gamma(\vec{x}, t)$  is done via a first-order approximation of the root of the maxima function,

$$\sum_{\alpha=1}^{27} \Delta h_\alpha \ln \left[ 1 + \frac{(1 - \beta\gamma) \Delta h_\alpha - (2\beta - 1) \Delta s_\alpha}{f_\alpha^{eq}} \right] \quad (20)$$

with a physical interpretation of selecting the value of  $\gamma$  that maximises the entropy of the post-collisional state. Here,  $\Delta s_\alpha$  and  $\Delta h_\alpha$  denote the deviations of  $s_\alpha$  and  $h_\alpha$  from equilibrium, respectively, or,

$$\Delta s_\alpha = s_\alpha - s_\alpha^{eq}, \quad \Delta h_\alpha = h_\alpha - h_\alpha^{eq} \quad (21)$$

or,

$$\Delta h_\alpha = f_\alpha - f_\alpha^{eq} - \Delta s_\alpha \quad (22)$$

In order to obtain an explicit solution to Eq. (20), the argument of small deviations about  $\ln(1+x) \approx x + \dots$ , and some algebraic manipulation, give the final expression for  $\gamma$ :

$$\gamma \approx \frac{1}{\beta} - \left( 2 - \frac{1}{\beta} \right) \frac{\langle \Delta s | \Delta h \rangle}{\langle \Delta h | \Delta h \rangle} \quad (23)$$

A point of clarification must be made about the notation for the entropic inner product  $\langle X | Y \rangle$ , where, departing from traditional bra-ket notation, the scalar product is also divided by the components of the equilibrium distribution,

$$\langle X | Y \rangle = \sum_{\alpha=1} \frac{X_\alpha Y_\alpha}{f_\alpha^{eq}} \quad (24)$$

To summarise the KBC model, the complete collision process can be performed in the below manner [19,22]:

- Computation of the conserved moments  $\rho$  and  $u_i$  [Eqs. (4) and (5)];
- Exact evaluation of the equilibrium distribution  $f_\alpha^{eq}(\rho, u_i)$  [Eq. (6)];
- Categorisation of the populations  $f_\alpha^{eq}$  and  $f_\alpha$ , explicitly calculating  $s$  and  $s^{eq}$  [Table 2];
- Evaluation of the deviations  $\Delta s_\alpha$ , and indirectly,  $\Delta h_\alpha$  [Eqs. (21) and (22)];
- Calculation of the entropic parameter  $\gamma$  [Eq. (23)];
- Final relaxation of the populations [Eqs. (12) and (15)].



### 2.1.3. Smagorinsky SRT LBM-LES

For this study, the SRT-LBGK is employed as a control model. For completeness, the algorithm is shown below:

$$f_\alpha(\vec{x} + \vec{e}_\alpha \delta_t, t + \delta_t) = f_\alpha(\vec{x}, t) - \frac{1}{\tau} [f_\alpha(\vec{x}, t) - f_\alpha^{eq}(\vec{x}, t)] \quad (25)$$

with the relaxation time  $\tau = \frac{1}{2\beta}$  being the shear-viscosity dependent term.

A well-known behavioural issue with the SRT-LBGK model is the onset of instabilities when  $\tau \rightarrow 0.5$ , which arises due to a too-high flow Reynolds number and/or with insufficient mesh resolution. This effectively limits a pure SRT-LBGK model to a DNS with a stiff computational limit on the uppermost achievable  $Re$ . Hence, in order to further stabilise the algorithm and/or incorporate a subgrid-scale model for large-eddy simulation, adjustments to the shear viscosity of the bulk fluid (and thus relaxation time) by modelling the local eddy viscosity  $\nu_t$  may be done such that

$$\nu_{total} = \nu + \nu_t \quad (26)$$

by which the Smagorinsky model [58] gives,

$$\nu_t = (C \Delta_x)^2 |S| \quad (27)$$

essentially coupling the viscosity to the strain rate via the magnitude of the strain-rate tensor  $|S|$ :

$$|S| = \frac{c_s^2}{2(C\Delta_x)^2} \left[ \sqrt{\nu^2 + \frac{2}{c_s^4} (C\Delta_x)^2 (s_{ij}s_{ij})^{\frac{1}{2}}} - \nu \right] \quad (28)$$

where, following literature values, the Smagorinsky coefficient  $C = 0.1$ , and in LBM-LES,  $\Delta_x$  is usually set to the lattice spacing  $\delta_x$ . Finally, the local strain-rate tensor  $s_{ij}$  (not to be confused with the  $s$ -components in Section 2.1.2) is given as [35,59]:

$$s_{ij} = \frac{1}{2} \left[ \frac{\partial u_i}{\partial x_j} + \frac{\partial u_j}{\partial x_i} \right] = \sum_{\alpha=1}^{27} e_{\alpha i} e_{\alpha j} (f_\alpha - f_\alpha^{eq}) \quad (29)$$

Combining the above and substituting for values of  $C$ ,  $\Delta_x$ , and  $c_s$  result in the final SRT-LBGK LES with Smagorinsky subgrid model reading as,

$$f_\alpha(\vec{x} + \vec{e}_\alpha \delta_t, t + \delta_t) = f_\alpha(\vec{x}, t) - \frac{1}{\tau_{eff}} [f_\alpha(\vec{x}, t) - f_\alpha^{eq}(\vec{x}, t)] \quad (30)$$

$$\tau_{eff}(\vec{x}, t) = 3 \left\{ \nu + \frac{1}{6} \left[ \sqrt{\nu^2 + 0.18 (s_{ij}s_{ij})^{\frac{1}{2}}} - \nu \right] \right\} + \frac{1}{2} \quad (31)$$

## 2.2. Computational domain and boundary conditions

### 2.2.1. Single square-grid (SSG) and turbulator grid geometry parameters

Following the work of Hurst and Vassilicos [41,42], space-filling grids may be characterised by a wake-interaction length scale along the streamwise direction  $x$  given as,

$$x^* = \frac{L_0^2}{t_0} \quad (32)$$

due to the crosswise square-root law growth of wakes downstream of the grid. Here,  $L_0$  is the length of the largest iteration (the sole iteration for SSGs), and  $t_0$  the lateral grid bar thickness. Eq. (32) has been proven to be sufficient to collapse the behaviour of various grids into a common profile of turbulence intensity ( $TI$ ) [41,42,60], with peak turbulence intensity achieved in the region of  $0.35 < x/x^* < 0.60$  depending on SFG iteration number [61]; for the SSG,  $TI$  peaks at a downstream position of  $x/x^* = 0.50$ .

To-date, two major versions of the single-square-grid have been documented in literature, the first being that of Zhou and collaborators at Nagoya University [49], and the second by Vassilicos and co-workers originating from Imperial College London [51,52]. For this study, the dimensions have been chosen to follow that by Vassilicos et al. This choice is based on two reasons; firstly, due to a more favourable  $\frac{L_0}{t_0}$  ratio which reduces the streamwise length requirements of the computational domain; and secondly, due to a more complete availability of experimental and DNS data with numerous points of comparison readily available.

Fig. 1 and Table 3 document the dimensions of the current SSG, with Fig. 1 further illustrating the relative lateral dimensions of the SSG in the domain, and Table 3 rescaling all dimensions in terms of convenient grid/lattice dimensions. The current dimensions provide a grid blockage ratio of  $\sigma_{SSG} = \frac{A_{SSG}}{A_{domain}} = 0.20$ . Finally, it is worth noting that while the streamwise grid thickness is not equivalent to previous studies, the equivalent streamwise thicknesses of the experimental [51] and DNS [52] studies also exhibit differences, with the current study having a grid aspect ratio in between the two studies. The agreement between the previously reported experimental and DNS studies indicates that the current influence of streamwise thickness may not be significant in the context of this study.



**Table 3**

Detailed dimensions of the single-square grid (SSG) and computational domain normalised by standard grid dimensions and in LB units.

SSG Dimension	$L_0$	$t_0$	Streamwise thickness	Computational working domain ( $L_y \times L_z \times L_x$ )
Normalised by $t_0$	$5.33t_0$	$1.00t_0$	$0.17t_0$	$10.7t_0 \times 10.7t_0 \times 75.0t_0$
Normalised by $L_0$	$1.00L_0$	$0.19L_0$	$0.03L_0$	$2.0L_0 \times 2.0L_0 \times 14.1L_0$
Lattice Units	32	6	1	$64 \times 64 \times 450$

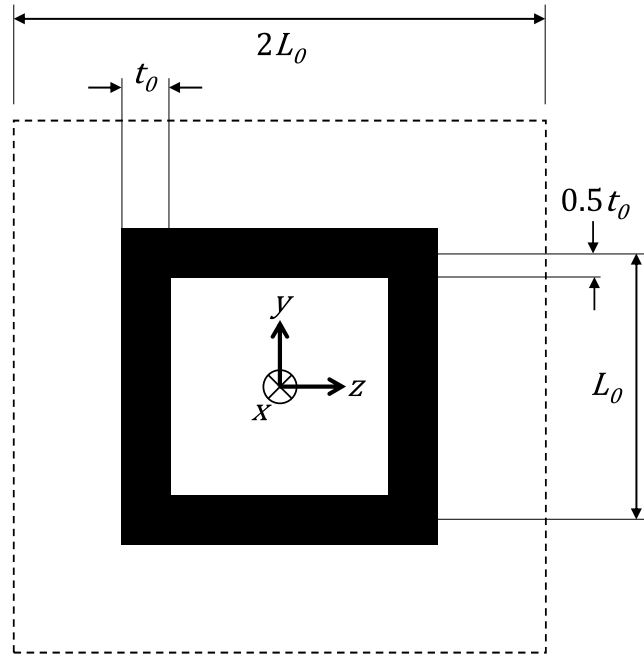


**Fig. 1.** Schematic of the SSG and associated dimensions, with relative lateral placement of the grid within the computational domain included (demarcated by dashed lines).

### 2.2.2. General domain information and boundary conditions

The SSG is placed along the central axis of a domain simulating a uniform one-dimensional flow past the grid in the streamwise direction. For this study, the origin is placed at the centre of the grid (Figs. 1 and 2a) with the Cartesian axes  $y$  and  $z$  being the axes in the lateral directions, and  $x$  being the streamwise direction axis. The domain is discretised into  $L_y \times L_z \times L_x = 64 \times 64 \times 600$  lattice cells, of which the upstream  $64 \times 64 \times 450$  cells contain flow-relevant settings (more information in Section 2.2.3). To ensure inlet conditions do not influence turbulence evolution behind the SSG, the SSG is placed at a conservative distance of 100 lattice units  $\approx 0.59x^*$  downstream of the virtual inlet. This provides a test section of 350 lattice units  $\approx 2.05x^*$  downstream of the grid for turbulence evolution to develop – however, in this study, data is only analysed in the region of  $0.00 \leq x/x^* \leq 1.50$ , with the remainder serving as a buffer for any effects from the outlet conditions. For future studies, the streamwise length may be shortened to reduce computational inefficiency.

Lateral boundaries of the domain are set to periodic conditions, in the same vein as previous literature [49,52] in order that wall effects do not influence turbulence evolution. Furthermore, this provides setup consistency compared to previous computational studies, such that any discrepancies may be attributed purely to the effect of the lattice-Boltzmann algorithms. Solid walls at the SSG–fluid interface obey the no-slip boundary condition, which is implemented in the LBM as the solid half-way bounce-back condition:

$$f_{\alpha}^*(\vec{x}, t) = f_{\alpha^-}^*(\vec{x}, t) \quad (33)$$

where  $\alpha^-$  denotes the index of the antiparallel direction vector to  $\alpha$ . Here, the half-way bounce-back condition is employed to bypass the considerations of viscosity-dependent wall boundaries for the full-way bounce-back schemes [12]. Due to the geometry of the current turbulator, no interpolation treatment is required for nodes at the solid–fluid interface, as all nodes are fully ‘wet’ or ‘dry’.

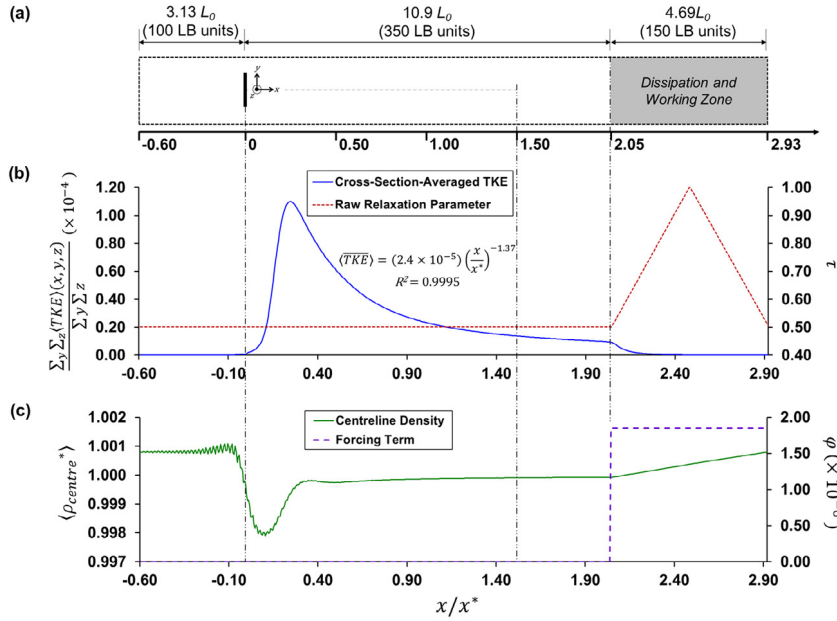


**Fig. 2.** Schematic (to-scale) of the computational domain. (b, c) present the satisfactory effects of the artificial dissipation/working zone, using the streamwise evolution of the cross sectional- and time-averaged TKE, and the centreline time-averaged density (left axes, solid lines). Streamwise values of the raw (i.e. pre-stabilised) relaxation parameter and simple forcing constant are also given for completeness in (b) and (c), respectively (right axes, dashed lines).

### 2.2.3. Streamwise inflow and outflow

A significant departure from the norm in this study may be observed in terms of the streamwise boundary conditions for inflow and outflow. A current limitation to high Reynolds-number LBM studies is the lack of a suitable formulation for outflow boundary conditions, where boundary pressure and velocity are not specified beforehand. The majority of current studies thus make do with a velocity inlet and a pressure outlet, with treatment required to prevent impinging pressure waves from fluctuations reflecting back into the domain [62]. While there has been some success in the above method in simulating turbulent flows [37], the effect of a fixed pressure outlet on the evolution of the upstream turbulence remains unknown; furthermore, a large degree of theoretical work remains to ensure that such boundary conditions are compatible with all classes of collision operator and LBM-LES algorithms. Here, we propose an interim alternative to enable high-Re LBM studies until such boundary conditions attain maturity.

In the spirit of recirculating wind tunnels, periodic boundaries in the streamwise direction are invoked, and a ‘working section’ at the tail end of the computational domain, which conditions the outgoing flow prior to recirculation, is included (refer Fig. 2a, shaded zone). This removes the earlier-mentioned need to specify a fixed pressure outlet condition and apply the associated nonreflective bounce-back conditions.

Obviously, some treatment must be applied to ensure that (i) the outflow fluctuations do not pollute the incoming flow profile (which, in general, is approximated as a uniform velocity or slug inflow, with low incoming turbulence intensity), and (ii) that the influence of pressure fluctuations are not streamed in downstream and upstream directions across the streamwise boundaries. For this study, the above is achieved by introducing a dissipation zone inside the working domain, where the relaxation parameter of the bulk fluid increases and then decreases along the streamwise direction following a ramp function (refer Fig. 2b, right axis, dashed lines). Namely:

$$\tau(x) = \frac{1}{2\beta(x)} = \begin{cases} \tau_0 + \frac{2(x-x_0)}{x_1-x_0} \tau_{peak}, & x_0 \leq x < \frac{x_1}{2} \\ \tau_0 + \frac{2(x_1-x)}{x_1-x_0} \tau_{peak}, & \frac{x_1}{2} \leq x \leq x_1 \end{cases} \quad (34)$$

where  $\tau_0$  is the unmodified relaxation time of the bulk fluid as calculated based on viscosity considerations,  $\tau_{peak}$  the peak value of the artificial relaxation time,  $x_0$  the coordinate of the streamwise position of the working zone inlet, and  $x_1$  that of the outlet. For this study,  $\tau_{peak}$  was set arbitrarily to 1.0.

Next, to enable continuous flow, simple forcing (ref. Eqs. (10) and (11)) is applied uniformly in the  $+x$ -direction inside this working section (refer Fig. 2c, right axis, dashed lines). A certain degree of trial-and-error is required for selection of the acceleration parameter  $\phi_i$ , corresponding to the desired inlet velocity and Reynolds number, but with careful interpolation, this is usually achieved in relatively few trials — furthermore, this method has also been employed in

**Table 4**

Computational runtime (with number of cores taken into account) for all simulations in the present study.

Simulation	Total CPU time (#cores $\times$ runtime), seconds	CPU Architecture
ELBM (KBC-N1)	$1.9 \times 10^6$	2 $\times$ Intel Xeon E5-2600
ELBM (KBC-N2)	$1.9 \times 10^6$	
ELBM (KBC-N3)	$2.6 \times 10^6$	
ELBM (KBC-N4)	$2.6 \times 10^6$	
SRT-LES LBM	$4.0 \times 10^6$	1 $\times$ Intel i7-6700K

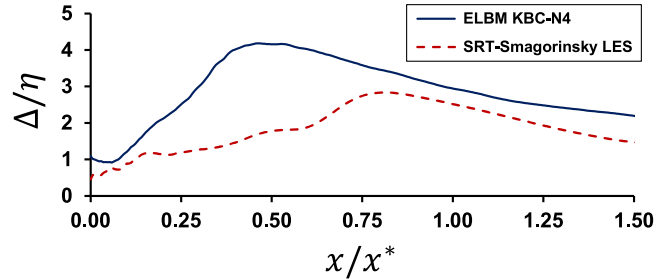


**Fig. 3.** Measure of streamwise under-resolution for the ELBM KBC-N4 and SRT-Smagorinsky SGS LES cases via the ratio of lattice unit length to the isotropically-calculated Kolmogorov length scale along the grid centreline.

previous body-force driven LBM studies [27,63]. For this study, it was found that a value of  $\varphi_x = 1.85 \times 10^{-6}$  achieved the target inlet flow velocity of  $U_\infty = 0.035$  (given in dimensionless lattice units). This corresponds to a flow Reynolds number of  $Re_{L_0} = 2.65 \times 10^3$  (normalised by the SSG bar length), equivalent to that by Paul et al.'s DNS study.

We justify preliminarily the effectiveness of the above as follows. Firstly, the effects of the working section (if any) are quantified by tracking the streamwise evolution of the turbulence kinetic energy in the entirety of the domain (Fig. 2b, left axis, solid line). It can be observed that the turbulence entering the dissipation zone is rapidly damped to negligible values before re-entering the inlet – for this study, the inlet turbulence, while not completely noiseless, is maintained at intensity levels less than 1% at all times, which is comparable to commercial-package RANS studies and experimental studies. Furthermore, the decay of the turbulence past the peak region is observed to follow a power-law in the range of  $0.70 \leq x/x^* \leq 1.40$  (refer inset correlation for Fig. 2b), qualitatively verifying that the turbulent behaviour modelled is in agreement with experimental findings [64,65]. This provides confidence for validation and reinforces the general agreement in results (Sections 3, 4, and 5) observed in the employed algorithms.

Second, we analyse the behaviour of the time-averaged density (LBM pressure analogue) along the SSG centreline (Fig. 2c, left axis, solid line). The pressure drop and subsequent recovery observed in the immediate downstream vicinity of the SSG is again in qualitative agreement with experimental and computational findings for similar studies – giving further confidence to proceed with this method.

At present, investigation into the suitability of other values of  $\tau_{peak}$ , let alone also the optimal length of  $x_1 - x_0$ , and the functions applicable to  $\tau(x)$  (e.g. asymptotic/power-law/step functions) have not been conducted. We opt for a linear trend in  $\tau(x)$  to model the 'spongy layers' adopted by contemporary non-reflecting boundary layer LBM studies [62] such that potential pressure wave reflections due to abrupt changes in relaxation are avoided. Additional optimisation studies are required to further this proposed workaround to maturity.

### 2.3. Data gathering and analysis

The domain is initialised with a uniform flow condition of  $u_x = 0.040$  throughout, and then allowed to evolve for three flow-through times assuming a target flow velocity of  $U_\infty = 0.035$  (see Section 2.2.3) – this corresponds to  $52 \times 10^3$  lattice time steps elapsed before recording of data. This is more conservative than previous literature, ensuring that transient effects do not skew the measured results. Finally, data is collected at a frequency of every 25 lattice time steps for an additional  $150 \times 10^3$  LB time steps (corresponding to  $\sim 8.65$  flow-through times). The total computational time required for each simulation is listed in Table 4. As the calculated minimal Kolmogorov time scale ( $\sim 100$  time steps) is at least four times longer than the sampling frequency, this ensures that the dataset satisfies the Nyquist criterion, and is also sufficiently converged for proper treatment of higher-order turbulence statistics and further analysis.

Being an under-resolved DNS/LES study, the lattice resolution is plotted in Fig. 3 for both the entropic and SRT-Smagorinsky cases. Here, the streamwise Kolmogorov length scale is estimated via the general formula of the isotropic scales:

$$\eta \approx \left[ \frac{\nu^2}{15 \langle \frac{\partial u}{\partial x} \rangle^2} \right]^{0.25} \quad (95)$$

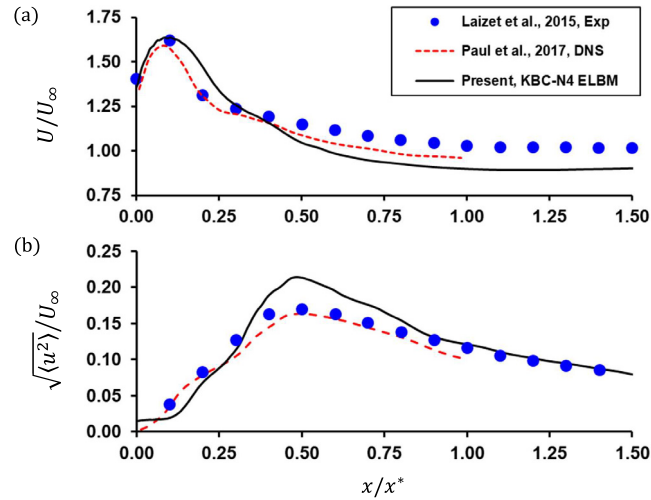


**Fig. 4.** Comparison of ELBM-predicted mean streamwise velocity (Fig. 4a) and streamwise turbulence intensity (Fig. 4b) along the SSG centreline with experimental (dotted) and most recent DNS (dashed) values.

For the KBC-N4 model, this estimate has been found to be in good agreement with the more elaborate treatment where dissipation is estimated by computing the inner product of the strain-rate tensor  $\epsilon = 2\nu \langle s_{ij}s_{ij} \rangle$ . Obvious disagreement between the KBC-N4 and the SRT-LES models is observed based on the calculated length scales, suggesting that the magnitude of the velocity gradients in the SRT-LES case has been underpredicted due to the added dissipation. Nevertheless, the evolution of the local resolution found in the KBC-N4 study is observed to obey the same trend as those reported by Paul et al. and Laizet et al. where the maximum under-resolution is observed at  $x/x^* = 0.50$ , before a gradual (linear-esque) improvement downstream. Hence, the trace of the KBC-N4 model agrees with previously reported literature and is a suitable benchmark for this study.

For all test cases, the turbulence evolution along the centreline of the single-square-grid is characterised and validated in terms of one-point statistics up to the fourth order (i.e. from mean velocity to fluctuation flatness), analysis of the budget of turbulence kinetic energy (following Tennekes and Lumley [66]), and energy spectra based on the time-autocorrelation of the streamwise fluctuations. For the KBC model, further analysis is performed based on the intermittency and strain product, which is discussed in the following section. Unless otherwise stated, all spatial derivatives have been evaluated using a second-order central difference scheme.

### 3. Comparison with literature — KBC model

The KBC-N4 model is chosen as the case to be benchmarked — as, by having the least influence from entropic stabilisation (ref. Table 2), it is expected to provide the most accurate estimate among the four proposed models.

#### 3.1. One-point statistics

For this study, comparison of one-point statistics is performed against experimental data from the original study of Laizet et al. [51], and the most recent DNS data from Paul et al. [52]. Analysis is first performed on the evolution of base turbulence statistics; namely, the time-averaged streamwise velocity,  $U = \langle u_x^* \rangle$  (here, in contrast to the abovementioned dimensionless nomenclature,  $u_i^*$  denotes the *instantaneous* velocity values), and turbulence intensity,  $TI_x = \sqrt{\langle u_x'^2 \rangle}/U$ , along the SSG centreline (Fig. 4). Here,  $u_x(x_i, t) = U(x_i) - u_x^*(x_i, t)$  denotes the fluctuating component as based on the standard Reynolds decomposition.

Previous literature has well-documented the behaviour of the above in the lee of both SSGs and SFGs. For the mean streamwise velocity, the constriction imposed by the grid accelerates the centreline flow to a peak in the vicinity of  $0.10 < x/x^* < 0.20$  before a gradual decay to the freestream value in the far field. As can be seen in Fig. 4a, the present study exhibits good agreement with both experimental and DNS data for  $0.00 < x/x^* < 0.50$ , with the current under-resolved simulation being able to capture the velocity peak just downstream of the grid. However, in the far field, the centreline velocity has a noticeable deficit from experimental values, transitioning to somewhat wake-like behaviour with the local mean velocity values being lower than that of the freestream. This discrepancy is not new, however, having also been recorded in the previous studies by Zhou et al. [49] and Paul et al. Specifically, they have shown that the choice of imposing periodicity in lateral boundary conditions is responsible for the difference in results, allowing for lateral outflow in contrast to experiment, where the flow is wall-bounded. In the present study, this difference is further exacerbated due

to the extended streamwise domain length in comparison to previous computational studies, explaining the larger relative deficit in mean velocity when contrasted against the data from Paul et al. Nevertheless, the satisfactory validation for the first-order mean velocity statistic, even with this relatively coarse discretisation, allows for the further investigation of higher-order statistics.

The intensity of turbulence fluctuations in the streamwise direction,  $Tl_x$  is a key performance indicator of passive turbulators. Unlike regular grids, which exhibit a rapid power-law decay of  $Tl_x$  downstream of the grid, the evolution of streamwise turbulence intensity in the lee of the SSG follows a production-peak-decay trend, with a peak of  $Tl_x$  occurring at a relatively far downstream distance of  $x/x^* = 0.50$ . This location is also used as a rough point of demarcation for the qualitative behaviour of turbulence, with the flow field downstream of the peak being characterised by the return of the turbulence to regular grid-produced decaying HIT, and the upstream zone characterised as a region influenced by intense, rare shedding events with large degrees of inhomogeneity and anisotropy.

Again, this behaviour for the SSG is well-documented, and comparison with the current study is given in Fig. 4b. It is worth noting that in order to account for the influence of the mean velocity deficit mentioned above, a slight departure of convention in the calculation of  $Tl_x$  is required. Namely, rather than normalising the absolute value of the r.m.s. fluctuations with the local mean velocity  $U(x)$ , the constant freestream mean velocity  $U_\infty = 0.035$  is used instead – this allows for a fair comparison of the prediction of the fluctuation strength, without the effects of  $U(x)$  incorporated into the performance measure – hence, for this study,  $Tl_x = \sqrt{\langle u_x^2 \rangle} / U_\infty$ . The same treatment has also been applied to the experimental and DNS literature values for comparison.

Good qualitative agreement for  $Tl_x$  is observed for the present study, as the peak location for  $Tl_x$  is in agreement with literature at  $x/x^* = 0.50$ , and full quantitative agreement is observed for  $x/x^* \geq 0.85$  in the downstream region, indicating, consistent with previous LBM studies, that the under-resolved LBM-DNS is able to capture the behaviour of decaying HIT. However, nearer to the SSG, the present study exhibits disagreement in two distinct zones – firstly, around the peak intensity zone of  $0.40 \leq x/x^* \leq 0.75$ , where an overprediction of  $Tl_x$  is found; and secondly, in the immediate downstream vicinity of the grid  $0.00 \leq x/x^* \leq 0.20$ , where a notable behaviour of underprediction with a ‘delay’ in turbulence intensity production is observed.

The discrepancy of  $Tl_x$  values in the peak region is most likely attributable to the coarse-discretisation effects of the present study, as, referring back to Fig. 3, this coincides with the region of most severe under-resolution with  $\Delta/\eta > 3$ . Hence, this suggests that a degree of subgrid-scale modelling is still required for under-resolved KBC-ELBM simulations to model turbulent dissipation at the small scales. Of course, a direct alternative would be to further refine the mesh resolution of the study; however, given the higher computational cost of the KBC-ELBM relative to other collision models, it remains an open question of whether the SRT-LBGK or constant-relaxation MRT models might be a better compromise for such high-resolution simulations. As this study aims to employ a LES-esque under-resolved approach (i.e. without the need for computationally expensive fully-resolved DNS) in order to make this a tractable problem without the need for high-performance computing architecture, we limit our mesh resolution to the current coarse scheme and leave the effects of mesh refinement for a further study.

The underprediction of production behaviour in the second region of disagreement, i.e. in the near field of the grid, however, cannot be attributed to the same factor of mesh resolution. This is further indicated by the apparent ‘delay’ in the rise of  $Tl_x$  which only occurs at a distance of about  $x/x^* = 0.10$  downstream of the SSG, rather than immediately after the grid as indicated by experiment and DNS values. This discrepancy is further investigated in Section 3.3 as the physical mechanisms behind such turbulence generation need to be investigated in detail.

For the sake of completeness in investigating the predicted one-point statistics, the statistical distributions of the streamwise fluctuations as they evolve along the centreline is calculated by measure of their third- and fourth-order moments of skewness and flatness. As a quick reminder, a Gaussian/normal distribution has skewness and flatness values of 0 and 3, respectively. While HIT in the far downstream region of grid turbulence generally has values close to (but never fully) that of a Gaussian distribution, literature has indicated the existence of extreme, rare deceleration events in the production region of both SSGs and SFGs, characterised by highly negative values of skewness and large flatness values.

The streamwise fluctuation skewness and flatness values, calculated as,

$$S_{u_x} = \frac{\langle u_x^3 \rangle}{\langle u_x^2 \rangle^{3/2}} \quad (36)$$

$$F_{u_x} = \frac{\langle u_x^4 \rangle}{\langle u_x^2 \rangle^2} \quad (37)$$

for the centreline along the SSG, is compared in Fig. 5a and 5b, respectively. Here, good agreement is again observed with experiment for both  $S_{u_x}$  and  $F_{u_x}$ , where, interestingly, the upstream peak in the vicinity of  $x/x^* = 0.10$  as found by experiment is also captured by the current simulation, and not by the DNS values; albeit with a slight downstream delay. It is hypothesised that this may be due to either the presence of a nonzero incoming background turbulence level in this study (which more closely resembles experimental conditions) or, due to a difference of pressure treatment in the DNS study – as it has been shown (and will also be discussed in the following subsections) that the turbulent behaviour in

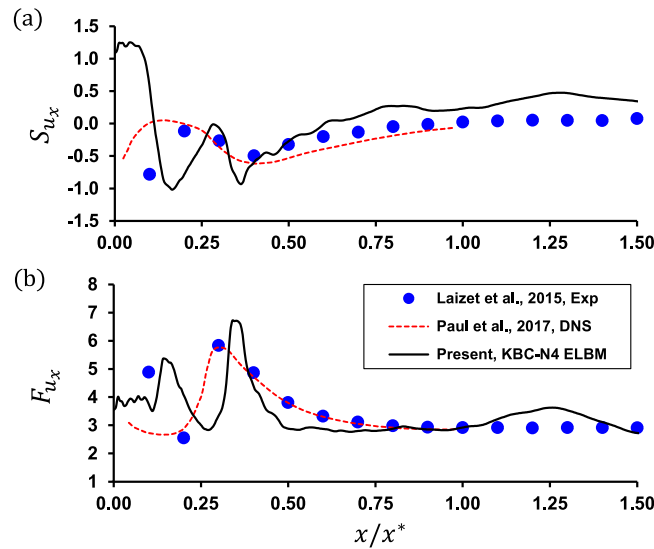


**Fig. 5.** Comparison of ELBM-predicted streamwise fluctuation skewness (Fig. 5a) and streamwise fluctuation flatness (Fig. 5b) values along the SSG centreline with experimental (dotted) and most recent DNS (dashed) values.

**Table 5**

Normalised root-mean-square errors (NRMSE) of the predicted turbulence statistic distributions along the centreline, compared to experimental values.

<i>NRMSE of centreline statistic prediction</i>	<i>Paul et al. 2017</i>	<i>Present, KBC-N4 ELBM</i>
Mean streamwise velocity	$2.97 \times 10^{-2}$	$4.74 \times 10^{-2}$
Streamwise turbulence intensity	$2.21 \times 10^{-2}$	$2.78 \times 10^{-2}$
Streamwise fluctuation skewness	$5.57 \times 10^{-2}$	$1.39 \times 10^{-1}$
Streamwise fluctuation flatness	$1.05 \times 10^{-1}$	$7.11 \times 10^{-2}$

that region is mainly influenced by pressure-driven events. Furthermore, the decay of the flatness values back to Gaussian behaviour after the second peak is more rapid in the current study as compared to literature — this may be explained by the overprediction of the growth of fluctuation strength in the peak region undercutting the values of the third- and fourth-order turbulence statistical moments.

A rough quantification of the errors in the predicted distributions of the centreline turbulence statistics is presented in Table 5. The deviations of the simulated values from literature experimental values are estimated using the discrete normalised root-mean-square error of the statistic, such that

$$NRMSE = \frac{\frac{1}{n} \sum_{i=1}^n \sqrt{[\phi(x_i) - \hat{\phi}(x_i)]^2}}{[\hat{\phi}(x)]_{max} - [\hat{\phi}(x)]_{min}} \quad (38)$$

where  $\phi(x_i)$  and  $\hat{\phi}(x_i)$ , respectively, denote the simulated and experimentally-determined test statistic value at downstream location  $x_i$ , and  $n$  the total number of data points from experiment used from the distribution. As expected, the high-resolution DNS results present the most accurate values except for the streamwise fluctuation flatness, as the peak at  $x/x^* = 0.10$  is not captured by the DNS. For the other statistics, the current study also presents relatively good agreement by having an NRMSE within a half-order of magnitude of that from the benchmark study, despite having a number of elements roughly 10 times lesser than the DNS.

Overall, the satisfactory agreement of centreline statistics up to the fourth order nonetheless indicates that the current KBC-ELBM model is well-suited to model turbulence beyond the standard HIT regime. This makes it a potentially viable simulation tool for contemporary turbulence mixing and heat transfer augmentation studies, where the accurate prediction of higher-order statistics is also required — which is captured in the current simulations. Furthermore, it is worth reiterating that the current results are achieved at a lattice discretisation much coarser than that of previous conventional DNS studies. This would indicate that the KBC-ELBM can also serve as a promising low-cost alternative for challenging turbulence simulations, accessible to a wider audience of researchers.



### 3.2. Turbulence kinetic energy budget

In order to ascertain that the physical mechanisms of turbulence generation and decay in the current study are also accurate, and that the resultant measured statistics are not influenced by numerical artefacts, further analysis is performed to compare the evolution of the budget of turbulence kinetic energy (*TKE*) along the SSG centreline. For this subsection and for Section 3.3, only the DNS values of Paul et al. are available for comparison.

Paul et al. have narrowed down the general six-term *TKE* budget as given by Tennekes and Lumley [66] to the following for turbulence along the SSG centreline:

$$\frac{\partial}{\partial t} \left[ \frac{1}{2} \langle u_i u_i \rangle \right] = -U_j \frac{\partial}{\partial x_j} \left[ \frac{1}{2} \langle u_i u_i \rangle \right] - \frac{\partial}{\partial x_j} \left[ \frac{1}{\rho} \langle u_j p \rangle \right] - \frac{\partial}{\partial x_j} \left[ \frac{1}{2} \langle u_i u_i u_j \rangle \right] - 2\nu \langle s_{ij} s_{ij} \rangle \quad (39)$$

where the terms on the RHS correspond respectively to convection by mean flow  $C_k$ , pressure work  $\pi_k$ , transport by turbulent fluctuations  $T_k$ , and viscous dissipation  $\epsilon_k$ . Production by the mean flow,  $P_k = -\langle u_i u_j \rangle S_{ij}$ , has been shown to be negligible for freestream-evolving turbulence, and for high-Reynolds numbers cases, viscous diffusion  $D_k = \frac{\partial}{\partial x_j} [2\nu \langle u_i s_{ij} \rangle]$  is also negligible. Here, as following standard notation,  $\rho$  is the fluid density,  $p$  the fluid pressure, and  $s_{ij} = \frac{1}{2} \left[ \frac{\partial u_i}{\partial x_j} + \frac{\partial u_j}{\partial x_i} \right]$  the fluctuation strain-rate tensor.

The budget terms as in Eq. (39) are calculated in the present study and compared with DNS data, as shown in Fig. 6a and b. The transport terms  $C_k$  and  $T_k$  are plotted in Fig. 6a, while the pressure work and dissipation terms  $\pi_k$  and  $\epsilon_k$  are plotted in Fig. 6b. Decent qualitative agreement is observed for the four dominant budget terms, indicating that the KBC-ELBM model does indeed recover the physical Navier–Stokes behaviour of SSG-generated turbulence, albeit without full quantitative agreement at under-resolution. Following the results by Paul et al. in the DNS study,  $\pi_k$  is the dominant production term in the near field for  $x/x^* \leq 0.15$ , before being superseded by  $T_k$  beyond  $x/x^* \geq 0.25$  as the growing wakes from the outlying SSG bars infiltrate the centreline. The transition of the mean convection term  $C_k$  from being a sink to a source in the vicinity of  $x/x^* = 0.60$  is also captured in the present study. Finally, while the dissipation term  $\epsilon_k$  has the best agreement with DNS values among the four budget terms, its magnitude is consistently underpredicted by the present study in comparison to the DNS data, further reinforcing the hypothesis that under-resolved entropic multirelaxation schemes require additional subgrid-scale modelling in order to fully capture the effects of turbulent dissipation. With regards to the quantitative agreement for the other three terms, the two regions of disagreement as prior-observed for turbulence intensity (Section 3.1) are also reflected here, with an underprediction of budget term magnitude for  $x/x^* \leq 0.15$ , and an overprediction due to resolution effects for  $0.40 \leq x/x^* \leq 0.75$ . For the latter, the spill-over of overproduction by the turbulent transport term is reflected by the sharp dip in  $\pi_k$  at  $x/x^* = 0.40$ . However, further analysis for the general underprediction of budget term magnitude in the near field is required — this is presented in the following section.

### 3.3. Turbulence in the near field — mean strain product analysis

Paul et al. have shown that in the near field of the SSG centreline, the evolution of the velocity-gradient tensor is fully attributable to the strain-rate tensor component, as the turbulent wakes from the surrounding bars have not yet infiltrated the centreline — only doing so in the region of  $x/x^* \approx 0.20$ . Hence, for the near field, the growth of *TKE* is not dependent on entropy, and is purely strain-rate dominated.

A similar budget analysis for the mean strain product,  $\frac{\partial}{\partial t} \left[ \frac{1}{2} \langle s_{ij} s_{ij} \rangle \right]$  can thus be performed following the work by Tsinober [67] and Paul, The near-field  $x/x^* \leq 0.20$  strain-rate budget is given by Paul as

$$\frac{\partial}{\partial t} \left[ \frac{1}{2} \langle s_{ij} s_{ij} \rangle \right] = - \left\langle s_{ij} \frac{\partial^2}{\partial x_i \partial x_j} p \right\rangle - U_k \frac{\partial}{\partial x_k} \left[ \frac{1}{2} \langle s_{ij} s_{ij} \rangle \right] - \frac{1}{2} \frac{\partial}{\partial x_k} [\langle u_k s_{ij} s_{ij} \rangle] - \langle s_{ij} s_{jk} s_{ki} \rangle \quad (40)$$

with the terms on the RHS corresponding respectively to the strain pressure Hessian  $\pi_s$ , the mean flow advection and turbulent fluctuation transport terms  $C_s$  and  $T_s$ , and, particular to the strain-rate dynamics, the strain self-amplification term  $P_s$ , where strain-rate is produced due to stretching by fluctuating strain. It was hypothesised by Zhou et al. and confirmed by Paul et al.'s DNS study that for  $x/x^* \leq 0.15$ , the dominant production term for strain-rate, and thus *TKE*, is  $\pi_s$ , with mean advection being the sink term in this region. Only further downstream, closer to the wake interaction zone, are transport by fluctuations and strain self-amplification activated, in that order.

Similar to Section 3.2, the budget comparison between the present study and the DNS data is given in Fig. 7, albeit with a modification in presentation order, where terms are grouped in sequence of order of activation downstream. Fig. 7a tracks the evolution of the first two terms which are activated, namely  $\pi_s$  and  $C_s$ , while Fig. 7b tracks  $T_s$  and  $P_s$ . It is immediately obvious that the underprediction of  $\pi_s$  by the present study is the main culprit for the delay in the prediction of turbulence intensity and kinetic energy observed in the previous sections, with a significantly smaller (but nonzero) magnitude as compared to the DNS — this is reflected by the equivalent under-prediction of  $C_s$  which serves to advect the strain product downstream. We surmise that this is due to the effect of compressibility in the classical LBM scheme. For this study, it is worth noting that the maximum Mach number based on peak flow velocity is less than  $Ma = 0.100$ , with the average Mach number based on inlet flow velocity being  $Ma_\infty = 0.061$ , and the maximum Mach number of



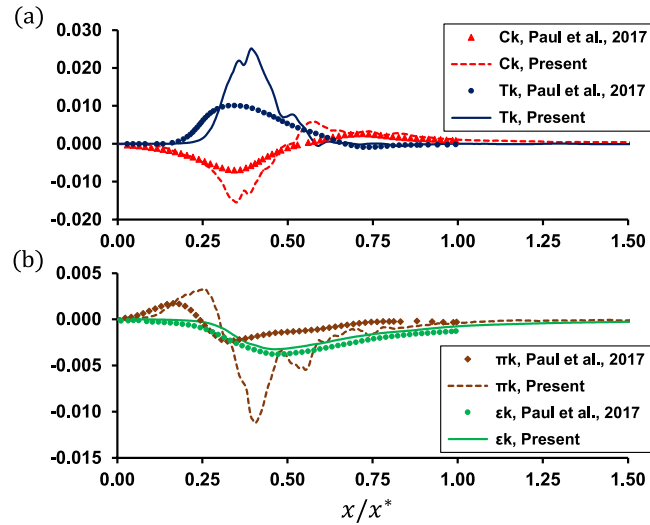


**Fig. 6.** Comparison of ELBM-predicted TKE budget terms (solid) along the SSG centreline with DNS (marker) values. (a) compares the transport terms (mean convection and turbulent transport), while (b) compares the effects of the pressure work and dissipation terms.

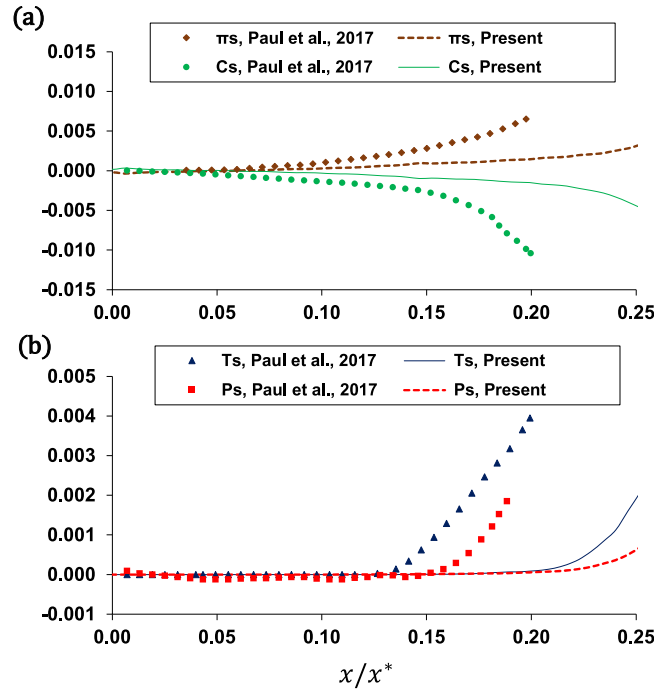


**Fig. 7.** Comparison of ELBM-predicted mean strain product budget terms (solid) along the SSG centreline with DNS (marker) values, in the SSG near field. Fig. 7a compares the terms activated earliest, while Fig. 7b compares the effects of the next two terms to be activated.

the fluctuations  $Ma_{li} = 0.012$ . Hence, further reduction of the macroscopic bulk velocity would not be sufficient to fully counteract this issue. This could warrant further LBM studies employing the ‘incompressible’ [68] formulations of the collision operator (albeit without entropic stabilisation, as current entropic models have not yet been expanded to this category) to turbulence where action of the pressure Hessian is dominant.

For completeness, the budget terms of  $T_s$  and  $P_s$  are also given in Fig. 7b. A clear delay in activation is again observed in comparison to the DNS data, with a lag of roughly  $0.05x/x^*$  downstream of the activation points as reported by DNS. This explains the delay in the rise of the  $T_k$  term in Fig. 6 — however, it is uncertain whether this is again an effect of the compressibility of the LBM, or, due to the effect of the entropic stabilisation of the current algorithm.

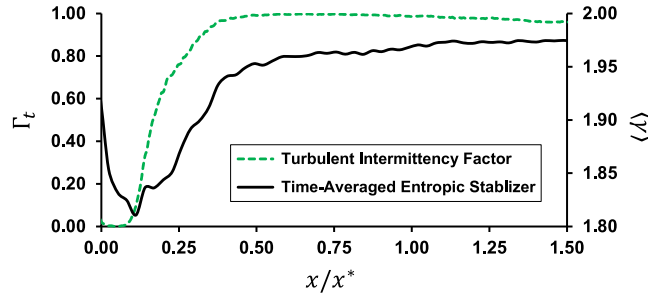


**Fig. 8.** Streamwise evolution of the turbulent intermittency factor (left axis, dashed line) and the time-averaged ELBM entropic stabiliser value (right axis, solid line), along the SSG centreline.

### 3.4. Behaviour of the KBC-N4 entropic stabiliser

In a similar vein to other entropically-stabilised LBM studies, a brief analysis is performed on the behaviour of the time-averaged entropic stabiliser and its evolution along the centreline, where the spatial trace passes through turbulent regimes with qualitatively different behaviour. This is shown in the right vertical axis for Fig. 8 (solid line). As a quick refresher, full Navier–Stokes behaviour is fully recovered only where the value of the entropic stabiliser,  $\gamma$  is equal to 2, with values less than this indicating that a net degree of entropic stabilisation is present.

It is first noticeable that the under-resolution of the study has forced  $\langle\gamma\rangle$  to be  $<2$  throughout the entirety of the centreline — this is not unexpected, as the current study requires the constant action of the entropic parameter in order to achieve a stable simulation at a coarse lattice discretisation. Moreover, it is also obvious, as shown in previous literature [19,21] that the effect of turbulence intensity magnitude and/or under-resolution is not correlated to the trend of  $\langle\gamma\rangle$  along the centreline, with the stabiliser only assuming a moderate value in the peak intensity and under-resolution zone of  $0.40 \leq x/x^* \leq 0.75$ . Rather, it is again in the near field, where irrotational and strain-rate-dominated flow exists, that  $\langle\gamma\rangle$  exhibits the greatest departure from Navier–Stokes behaviour, with the average value exhibiting a minimum of  $\langle\gamma\rangle = 1.81$  at  $x/x^* = 0.10$ .

The closest correlation between  $\langle\gamma\rangle$  and turbulent behaviour is observed when the plot of turbulent intermittency is overlaid with that of the stabiliser time-averaged value (Fig. 8, left axis, dashed line). This is a measure of the proportion of time in which a point in the flow field experiences turbulent behaviour in contrast to irrotational flow, and is usually expressed as

$$\Gamma_t(x) = \mathbb{P}[|\omega|(x, t) \geq |\omega|_{th}] \quad (41)$$

where, to avoid confusion between the nomenclature of the entropic stabiliser and intermittency, the traditional use of the lowercase Greek gamma here is replaced with the uppercase  $\Gamma_t$  and subscripted with  $t$  to distinguish from the entropic parameter. Here,  $|\omega| = \sqrt{\omega_i \omega_i}$  is simply the magnitude of the fluctuation vorticity vector  $\omega_i = \epsilon_{ijk} \frac{\partial u_k}{\partial x_j}$ , with  $\epsilon_{ijk}$  being the standard Levi-Civita symbol. For this study,  $|\omega|_{th}$  was determined following the method outlined by Paul et al. [54], and  $|\omega|_{th}$  was set as  $5 \times 10^{-4}$  for this study.

Referring to Fig. 8, it is worth noting that a correlation between  $\Gamma_t$  and  $\langle\gamma\rangle$  is observed for  $x/x^* > 0.10$ . The minimum point of  $\langle\gamma\rangle$  closely coincides with the lift-off point of  $\Gamma_t$  to nonzero values, after which, better recovery of Navier–Stokes behaviour is observed even as the flow field becomes more fully turbulent downstream. This is surprising as a high degree of entropic stabilisation is required for regions experiencing irrotational behaviour, as can be seen in the region of  $0.00 \leq x/x^* \leq 0.25$ . Hence, it is hypothesised that it is not so much the inherent strength of the turbulence, but rather, the intensity and frequency of transitions between irrotational and fully developed turbulence that has the most influence on the entropic parameter, and thus the stability of ELBM simulations in general.

### 3.5. Spectra

We close this section with a brief examination of the energy spectra for the streamwise fluctuation correlations along the centreline of the SSG. The spectra are obtained by performing a Welch power-spectral density estimate employing a Hanning window with one-third signal length on the streamwise autocorrelation vector:

$$R_{xx}(T) = \langle u'_x(t) u'_x(t+T) \rangle \quad (42)$$

with leftover noise (observed especially in the high-frequencies) smoothened by a Savitzky–Golay filter of polynomial degree 3. Six points along the SSG centreline are probed, namely,  $x/x^* = 0.10$  (early production, irrotational),  $x/x^* > 0.30$  (late production, turbulent),  $x/x^* > 0.50$  (peak),  $x/x^* > 0.80$  (early decay), as well as  $x/x^* > 1.10$  and  $x/x^* > 1.50$  (late decay and domain limit). For ease of presentation, the magnitude of the fluctuations has been rescaled such that  $u'_x = \frac{u_x}{U_\infty}$ , as the raw dimensionless results for  $u_x$  result in very small values for  $R_{xx}$  and  $E_{uu}$ .

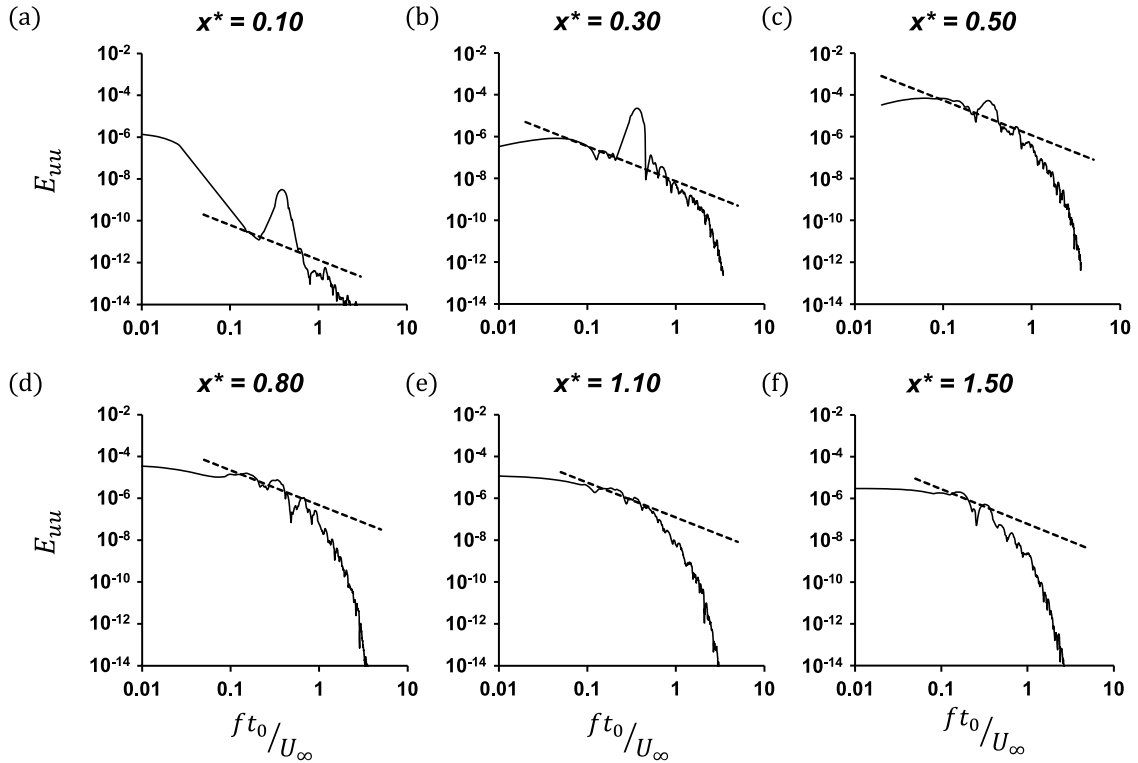


**Fig. 9.** Streamwise correlation energy spectra along the grid centreline as obtained by the KBC-N4 ELBM simulation at selected points downstream of the SSG, inclusive of the production, peak, and decay regions. Dashed lines have a  $-5/3$  slope for ease of comparison to the quasi  $-5/3^{rd}$  Kolmogorov scaling law as reported in previous studies.

The spectra for the above are documented in Fig. 9. Two major points of qualitative agreement are again observed with literature: firstly, that of a strong vortex shedding signature in the production region, signified by the bumps in the spectra for  $x/x^* = 0.10$  and  $x/x^* = 0.30$ . This behaviour has been well-documented in both experimental and DNS studies for turbulence in the lee of both SSGs and SFGs. Secondly is the existence of a five-thirds Kolmogorov-esque scaling law, also found in previous results employing both SFGs and SFGs, even though the turbulence in this region does not satisfy the isotropy and homogeneity requirement of Kolmogorov's hypothesis. Again, in line with Paul et al.'s DNS data, this agreement with the quasi-5/3rd's law is strongest in the near field, with the scaling spanning roughly a half-decade of frequencies for  $0.10 \leq x/x^* \leq 0.50$ , before degrading in the far field as shown in the bottom row of Fig. 9. While the absence of non-dimensionality in  $E_{uu}$  for previous studies precludes a one-to-one quantitative comparison, the excellent qualitative agreement for energy spectral behaviour as predicted by the KBC-N4 ELBM model further establishes, from a separate perspective, that the underlying physics of turbulence evolution in the current study is solid. This is especially useful in contemporary receptivity theory-based turbulent transport studies [69] where the need of identifying dominant frequencies emanating from turbulators is key to determining transfer/mixing performance.

#### 4. Comparison with the SRT-LES control model

##### 4.1. One-point statistics

Similar to the analysis performed in Section 3.1, the evolution of one-point turbulence statistics along the centreline is analysed for the control run employing the SRT-LES operator with Smagorinsky subgrid modelling. Here, the mean streamwise velocity and turbulence intensity are given in Fig. 10a and 10b respectively, while the higher-order moments of skewness and flatness are presented in Fig. 11a and b. For ease of comparison, the DNS data of Paul et al. has been omitted for this subsection.

It is obvious from the outset that the data from the control simulation do not agree either quantitatively or qualitatively with experimental values, when run at the same coarse resolution as that of the KBC-N4 model. For Fig. 10, the extended range of jet-like behaviour observed in the plot of mean streamwise velocity, coupled with the corresponding significant delay and truncation of the peak in turbulence intensity in Fig. 10b, indicate the over-viscous action of the SGS model in the production and peak regions of the grid. In the far field, where the LES-predicted flow transitions to wake behaviour

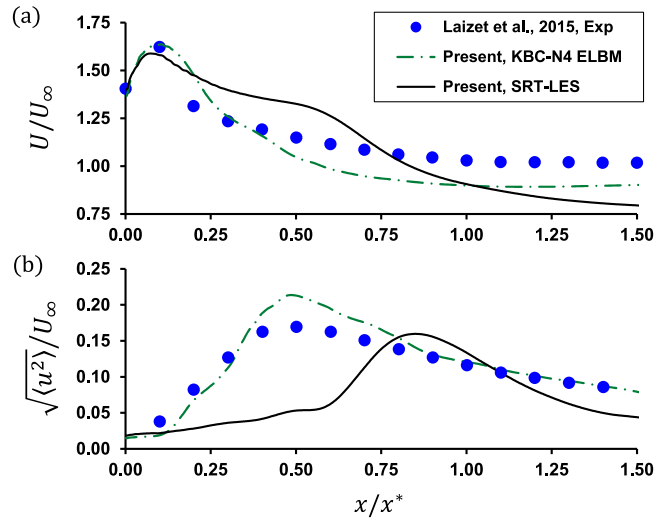


**Fig. 10.** Comparison of SRT-Smagorinsky LES-predicted mean streamwise velocity (a) and streamwise turbulence intensity (b) along the SSG centreline with experimental (dotted) and most recent DNS (dashed) values.

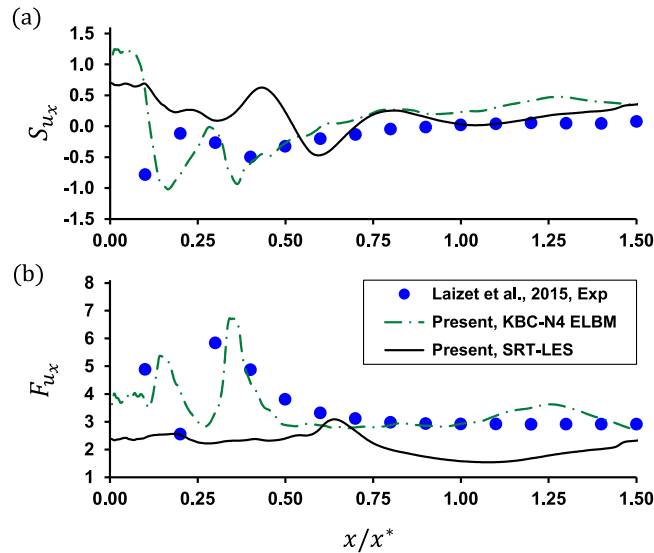


**Fig. 11.** Comparison of SRT-Smagorinsky LES-predicted streamwise fluctuation skewness (a) and streamwise fluctuation flatness (b) values along the SSG centreline with experimental (dotted) and most recent DNS (dashed) values.

and turbulence decay, decent recovery of the freestream decaying fluctuations is obtainable given the low-intensity, quasi-homogeneous and isotropic nature of the turbulence in that region.

The parallel in spatial location ( $x/x^* \approx 0.60$ ) between the transition to wake flow in Fig. 10a and the beginning of the significant increase in  $Tl_x$  production in Fig. 10b suggest a highly delayed onset of wake interaction from the surrounding bars of the SSG, well beyond the literature-reported values of  $0.20 \leq x/x^* \leq 0.40$ . This is further supported by the slight dip and rise in  $S_{u_x}$  and  $F_{u_x}$  respectively at the same location (Fig. 11). As discussed in the previous section, the presence of shedding and intermittent intense events at this point heralds the beginnings of wake interaction; however, the magnitude of these rare events is also greatly underpredicted by the current LES model. Again, this is most likely due to subgrid-scale assumptions dampening out such intense events by subjecting the local relaxation directly to the magnitude of the local strain-rate. In contrast, it is remarkable the under-resolved KBC-N4 simulations achieve such satisfactory agreement with the literature at this coarse resolution.

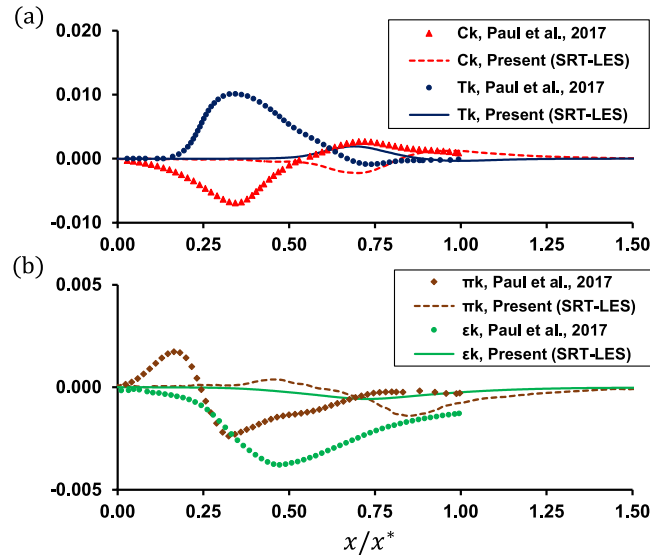


**Fig. 12.** Comparison of SRT-Smagorinsky LES-predicted turbulent kinetic energy budget terms (solid) along the SSG with DNS (marker) values. (a) compares the transport terms (mean convection and turbulent transport), while (b) compares the effects of the pressure work and dissipation terms.

#### 4.2. Turbulence kinetic energy budget

To further verify the hypothesised delay of wake interaction along the centreline, and to also examine if the aforementioned compressibility effects in the near field are present in the current SRT-LES model, an equivalent budget of turbulence kinetic energy (following that in Section 3.2) is performed for the current simulation, and is presented in Fig. 12; again, transport terms are given in Fig. 12a while pressure work and dissipation is presented in Fig. 12b.

Examination of the evolution of  $C_k$  and  $T_k$  confirms the delayed onset of wake interaction, as the SRT-LES predicted traces of the two budget terms are noticeably shifted downstream, and are lower in magnitude by roughly fourfold when compared with the DNS data. A similar trend is observed for  $\pi_k$  and  $\epsilon_k$  in Fig. 12b; however, the underprediction of  $\pi_k$  is not as severe as its transport term cousins. Again, similar to Fig. 6b,  $\pi_k$  does not lift off from nonzero values in the extreme near field of the turbulator, confirming the hypothesis that the underprediction effect in the pressure-driven region of the flow fluctuation field is not an artefact of the entropic stabilisation, and is a result of the pseudo-compressibility of the LBM. For the SRT-LES case, this is further exacerbated ( $\pi_k$  does not lift-off until roughly  $x/x^* = 0.20$ ) as the relaxation of bulk-viscosity driven events is also slaved to the subgrid model due to a single relaxation time.

#### 4.3. Comparison with the KBC model

While analysis of the centreline statistics has highlighted the differences in the physical mechanisms of turbulence generation between the partial-entropically stabilised and eddy-viscosity LBM-LES collision models for this study, a global comparison of the flow field between the two models would serve to encapsulate the abovementioned discrepancies to a single convenient point of reference. As such, a two-dimensional contour slice of the time-averaged streamwise mean velocity field and the time-averaged normalised turbulence intensity (refer Section 3.1 for normalisation details) is presented in Figs. 13a and 13b respectively, where results from the KBC-N4 simulation are positioned top and that of the SRT-LES positioned bottom. Here, the choice of normalising  $T_{ix}$  by  $U_\infty$  for this study is further justified as this allows for calculation of finite intensities even in the low-velocity recirculation regions in the lee of the SSG bars.

It can be summarised that the action of the Smagorinsky-SGS model is to retard the growth of the lateral wakes from the turbulator into the surrounding flow, firstly due to excessive dissipation at the solid-fluid boundary when the magnitude of local strain-rate is large (Fig. 13b), and secondly in the freestream where the irrotational zone separating the jet-like behaviour past the grid opening and the wakes behind the bars is artificially extended due to higher effective viscosities precluding effective turbulent mixing and transport (Figs. 12a and 13a).

This justifies the efforts of the KBC model in isolating the shear viscosity (and the bulk viscosity) parameter from dissipation or entropic control, allowing for much greater accuracy in flow field simulation even at a relatively coarse resolution, in contrast to schemes with the effective shear relaxation is also modified. While this has been shown to be the case for the Smagorinsky subgrid model, it remains an open question of whether the SRT-ELBM, with its capability to backscatter turbulent kinetic energy, will encounter a similar issue.

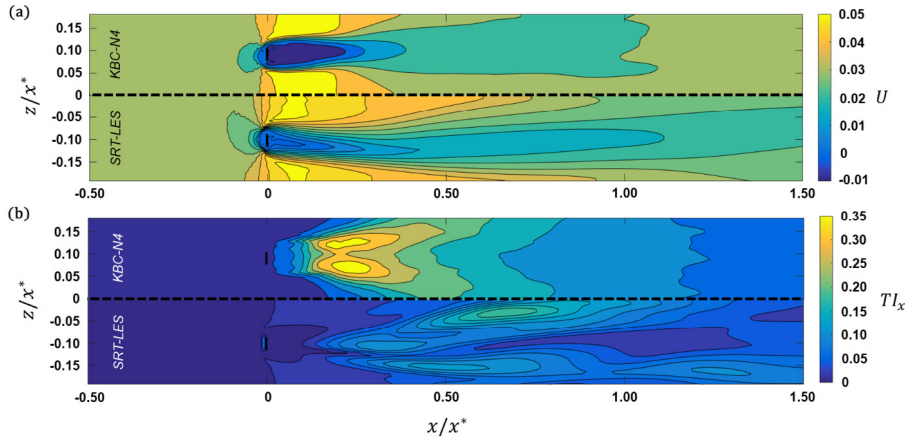


**Fig. 13.** Mean streamwise velocity contours (Fig. 13a) and streamwise turbulence intensity contours (Fig. 13b) for a 2D slice along the centre plane ( $y = 0$ ) of the simulated domain, with values from the KBC-N4 simulation plotted top and that from the SRT-Smagorinsky LES simulation plotted bottom.

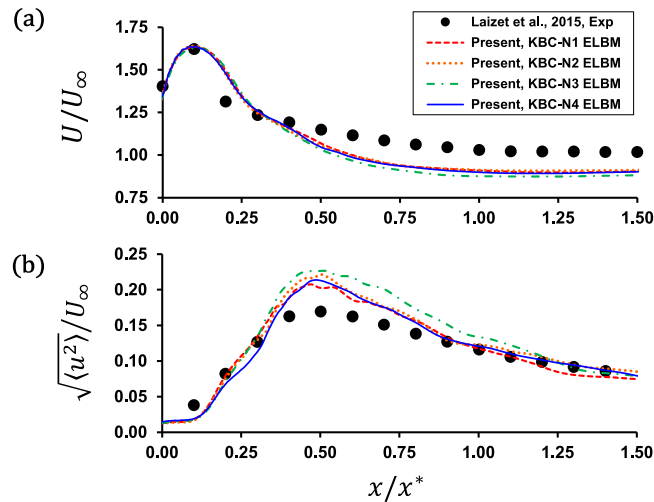


**Fig. 14.** Effect of the extent of entropic stabilisation (N1–N4) on KBC-ELBM turbulence statistics prediction performance, using the mean streamwise velocities (a) and streamwise turbulence intensities (b) along the SSG centreline as indicators.

## 5. Effect of KBC N1–N4 models

In the previous literature, only the KBC-N4 model has been employed as a reference point in comparing the veracity of the entropic multirelaxation LBM to experiment and traditional Navier–Stokes solver studies. However, the need to perform a large degree of moment categorisation to fully isolate the s-components for the N4 case (refer Tables 2 and 4) results in increased computational overhead — and it can be questioned whether the N1–N3 models with higher degrees of entropic stabilisation (and hence, less computational effort) may serve as a good compromise for increased efficiency with acceptable trade-off in terms of accuracy.

In order to assess the viability of the KBC N1–N3 models for this test case, and to also further examine the behaviour of the entropic parameter when subjected to varying degrees of moment stabilisation, three additional equivalent test cases were performed for turbulence generated by the SSG, with the sole point of difference being the collision model employed (KBC N1, N2, and N3). Results from these cases are contrasted with the KBC-N4 model in terms of one-point statistics, and the evolution of the gamma entropic parameters along the centreline are also examined.

### 5.1. One-point statistics

Following the layout of the previous sections of this paper, Fig. 14 documents the evolution of the mean velocity and streamwise turbulence intensity along the SSG centreline, while Fig. 15 tracks the streamwise fluctuation skewness

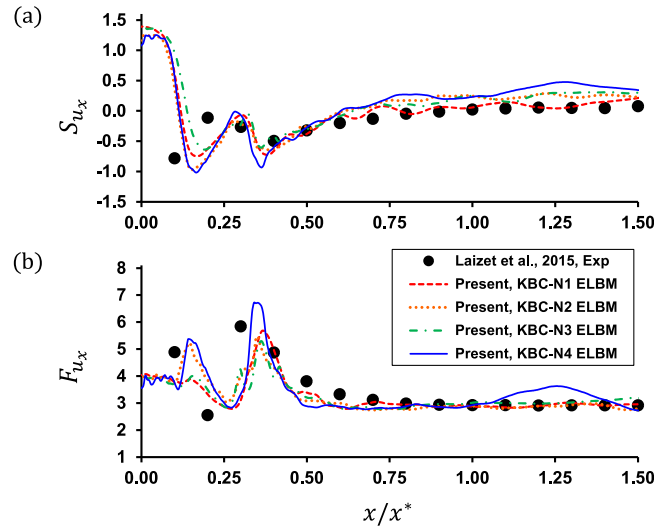


**Fig. 15.** Effect of the extent of entropic stabilisation (N1–N4) on KBC-ELBM turbulence statistics prediction performance, using the streamwise turbulent fluctuation skewness (a) and streamwise turbulent fluctuation flatness (b) along the SSG centreline as indicators.

and flatness along the same spatial trace, for the simulations employing the KBC-N1 through -N4 models. Here, only the experimental values of Laizet et al. are used for comparison, to preserve clarity of presentation.

Referring to Fig. 14a, it can be seen that little variation is observed among the four models for the mean streamwise centreline velocity. This is expected, as all models should preserve continuity — more so as the zeroth-order moments are not subject to entropic control and are conserved for any LB scheme. However, upon examination of the predicted turbulence intensity in Fig. 14b, the effect of the differing degrees of entropic stabilisation between models begins to be apparent, mainly in the region of severe under-resolution as detailed in the previous sections for  $0.40 \leq x/x^* \leq 0.75$ . This indicates that the effect of partial entropic stabilisation does indeed serve as a form of subgrid modelling, even though the base value of shear viscosity for all models is equivalent. Moreover, as all models exhibit an overprediction of turbulent energy in this region, this further reinforces the premise that a refinement of the subgrid model is required in tandem with the KBC-ELBM to enhance the accuracy of the model in coarsely-resolved simulations. In the near-field for  $0.00 \leq x/x^* \leq 0.20$ , all models exhibit surprisingly consistent behaviour with each other in terms of the under-prediction of turbulent intensity as documented in Section 3. This further indicates that this phenomenon is not an effect of the entropic collision model, but is prevalent to compressible LB schemes in general. Finally, of the four models, it is worth noting that the KBC-N3 model is the least accurate, being less so than the N1 and N2 models which have higher degrees of stabilisation.

The differences between the four models become most prominent when expanding the analysis to the third- and fourth-order statistics as shown in Fig. 15. Here, a distinct underprediction for the streamwise fluctuation skewness  $S_{u_x}$  is seen in the first dip around  $0.15 \leq x/x^* \leq 0.20$  for the N1 and N3 models. This is even more pronounced when a comparison to the corresponding peak for  $F_{u_x}$  is made, where the N1 and N3 models do not exhibit any significant rise in flatness at all. For both skewness and flatness, more accurate results are shown by the N2 and N4 schemes — while this is understandable for the N4 scheme, having the least degree of stabilisation, the improved performance of the N2 model in comparison to the N3 scheme, coupled with the poor overall accuracy of the N3 model, requires further discussion.

Recalling that intense events in the near field are due to pressure effects and the action of the pressure Hessian (Sections 3.2, 3.3), it can be seen that phenomena related to the fluid bulk viscosity play a key role in the SSG near-field turbulence. On the other hand, by also noting that the KBC-N1 and -N3 models set the trace of the stress tensor,  $T$  under entropic control, resulting in a fluctuating bulk viscosity, it can be surmised that entropic stabilisation of the bulk viscosity-related moments artificially dampen out turbulent fluctuations of this nature, explaining the poor performance of the  $T$ -stabilised models in this one-point statistics analysis. In general, this indicates that the MRT and entropic MRT schemes must exercise caution when adjusting for bulk viscosity relaxation, as this is not a ‘free-tuning parameter’ — especially for studies involving turbulence with the above nature.

The KBC-N2 model, by leaving the trace of the stress tensor unaffected, provides comparable performance to the N4 scheme, and may serve as a good compromise for applications where speed is valued over some trade-off in accuracy. For this test case, the only significant result where the N4 scheme outperforms the N2 formulation is in the prediction of second flatness peak at  $x/x^* = 0.30$ . This is surmised as being due to the complex interplay between wake interactions and pressure effects in this region, where the effect of the third-order moments and higher is also prevalent.



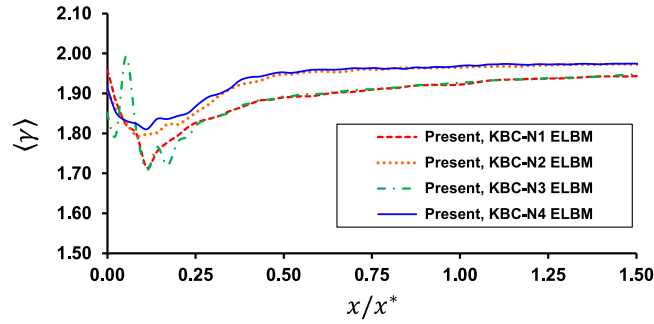


**Fig. 16.** Streamwise evolution of the time-averaged entropic stabiliser value for the KBC-N1 to KBC-N4 models along the SSG centreline.

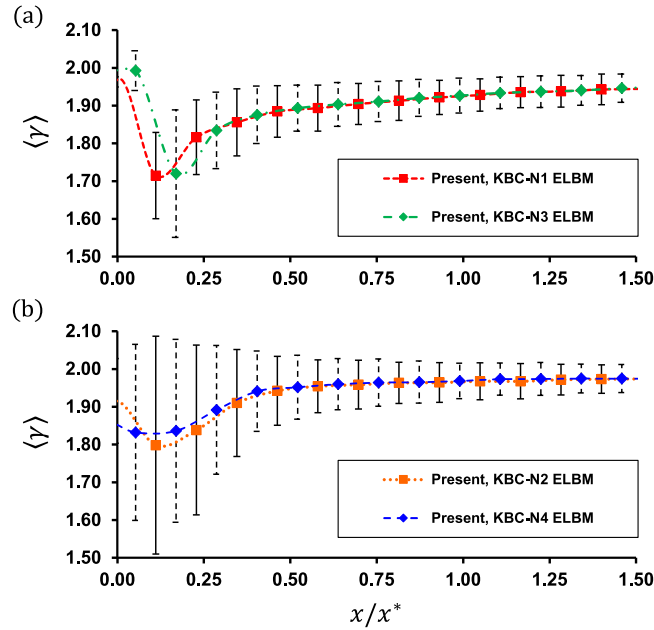


**Fig. 17.** Streamwise evolution of the time-averaged entropic stabiliser value for the KBC-N1 and KBC-N3 models (Fig. 17a) as well as the KBC-N2 and KBC-N4 models (Fig. 17b), along the SSG centreline. RMS values of the stabiliser fluctuations are denoted by the solid (KBC-N1, N2) and dashed (KBC-N3, N4) error bars.

## 5.2. Behaviour of the entropic stabilisers

We close this section with a more detailed comparison and analysis of the distribution of the gamma entropic stabiliser along the SSG centreline, where for clarity of presentation, the time-averaged value of  $\gamma$  is plotted for every five lattice nodes along  $x$  in Fig. 16, and the magnitude of r.m.s. fluctuations for  $\gamma$  is plotted about the time-averaged value (vertical error bars) for every ten lattice nodes along  $x$  in Fig. 17.

The distinct separation for the trajectories of  $\langle \gamma \rangle$  between the  $T$ -stabilised (N1 and N3) and non- $T$ -stabilised (N2-N4) models as seen in Fig. 16 further cement the fact that bulk viscosity effects play a key role in turbulence evolution behind the SSG, and this extends throughout the entirety of the centreline domain, with the N1 and N3 models exhibiting lower values of  $\langle \gamma \rangle$  for all points. Interestingly, the choice of stabilising the trace of the stress tensor while leaving the third-order moments unaffected results in a wildly-fluctuating  $\gamma$ -parameter for the N3 model in the near field of the SSG — this is shown by the spurious peak of the N3 trace at  $x/x^* = 0.10$ . As expected, the time-averaged  $\gamma$  value for the N4 model is closest to 2 in comparison to all other models, giving closest approximation to Navier–Stokes behaviour.

Finally, by briefly examining the r.m.s. fluctuations of  $\gamma$  in time for the N1/N3 (Fig. 17a) and N2/N4 models (Fig. 17b), it can be seen that for the most part, the entropic parameter for the N1/N3 models and the N2/N4 models exhibit similar behaviour respectively within the two subclasses. In general, similar to the region of net departure from Navier–Stokes behaviour in Fig. 16, the fluctuations are the most intense in the near field of the SSG, and not at  $x/x^* = 0.50$  where peak turbulence intensity is located. Here, the fluctuations for the N2/N4 models are more intense than their

N1/N3 counterparts, indicating larger potential for instability and entropy conservation violation by the higher-order moments that exclude  $T$  — this agrees with literature which pins the effect of instability in MRT schemes on such ‘ghost’ moments. Overall, this also shows that the entropic stabiliser plays an active role in constantly stabilising these under-resolved simulations, and cannot be pinned to a constant value unlike its constant-relaxation-value MRT counterparts. This indicates further promise for such partial algebraic MRT relaxation schemes, where the increased computational overhead in calculating the relaxation parameter is justified by the attainment of higher flow Reynolds numbers, whilst being stable and (in the context of this study) qualitatively accurate.

## 6. Conclusions

This study reports the first successful employment of the partial-entropically-stabilised multirelaxation time lattice-Boltzmann model proposed by Karlin and co-workers (termed the KBC-ELBM model) to an under-resolved DNS of turbulence not yet discussed in previous LB literature — namely, that in the lee of a space-filling single-square grid. Here, the large lateral grid dimensions relative to the flow domain magnify the size of the non-homogeneous, anisotropic production region — hence, beyond adding a rare case of LB-simulated grid-generated turbulence to the current literature, this test case also serves to examine the limits of both the entropic KBC collision model and the classical quasi-compressible LBM algorithm in simulating nonclassical turbulence studies.

The inclusion of a novel ‘working zone’ in the rear of the computational domain, with the dual aim of maintaining flow circulation and residual turbulence dissipation, allows for the simulation of one-dimensional turbulent flows past obstacles regardless of collision model employed. This bypasses the need to employ nonreflective pressure outlet boundary conditions, and also circumvents the current stability considerations for open-type BC’s. Thus, it is proposed that the current method may serve as an interim compromise solution, until the mathematical framework for outflow boundary conditions that may admit entropic operators is formally determined. The suitability of the above method is qualitatively validated by examination of the global flow field behaviour, specifically, by examining the decay of turbulence kinetic energy and the variation of the pressure-analogue density along the centreline.

The simulation of SSG-generated flows by the natural-moment KBC-ELBM models are compared and validated against both experimental and DNS literature data, with the SRT-Smagorinsky LES collision model serving as a control case. The KBC-N4 ELBM model exhibits very good qualitative agreement in terms of one-point statistics, budget of turbulence kinetic energy, and streamwise energy spectra along the SSG centreline when compared with literature, enabling the KBC-ELBM model to serve as a promising alternative to DNS studies for turbulence behind space-filling grids. In comparison, the SRT-LES case fails to attain both quantitative and qualitative agreement with literature, as the overprediction of eddy viscosity retards the growth of wakes generated by the SSG bars into the freestream, resulting in truncated and delayed values of the one-point statistics as well as the turbulence kinetic energy budget terms.

Quantitative disagreement between literature and the current study for streamwise turbulence intensity and turbulence kinetic energy evolution in the most severely under-resolved zones ( $0.40 \leq x/x^* \leq 0.75$ ) indicate that a subgrid model may still be required for the KBC-ELBM model, as, while it leaves the shear viscosity parameter unmodified in contrast to the entropic SRT model, insufficient turbulent dissipation is modelled at the subgrid scale for coarse resolutions ( $\Delta/\eta > 3$ ), and calls for further treatment for the model to serve as a satisfactory LES scheme in such setups and regions.

Moreover, in the general context of compressible LB schemes, caution must be taken when simulating turbulence produced by pressure work as well as strain-rate by pressure Hessian, indicated by the underprediction of streamwise turbulence intensity in the extreme near field of the SSG. As this is a common issue among all KBC models, as well as the SRT-LES model, the effect of collision model can be safely excluded as being a potential factor for this discrepancy.

Finally, by comparing the predictions of the KBC-N1 to -N4 models with varying degrees of entropic control over moment order, a quasi-physical understanding of the effect of entropic stabilisation on turbulence evolution behind the SSG is obtained. Beyond leaving the shear viscosity unaffected, it is shown that moments relating to the trace of the stress tensor should also not be subject to entropic stabilisation. This is evidenced by the superior performance of the KBC-N4, and more significantly, the KBC-N2 model, over the N1 and N3 models — measured in terms of both the apparent one-point statistics, and by analysis of the time-averaged degree of departure of the corresponding entropic stabiliser from the Navier–Stokes equivalent value. This also provides a certain degree of insight into turbulence modelling, especially for applications pertaining to the production region of space-filling grid-generated turbulence.

Future work may be done to quantify the effect of mesh resolution on the performance of the LBM-LES and under-resolved KBC-ELBM DNS models, as the lattice resolution was a fixed variable for this study, with obvious penalties in accuracy reported in regions of severe under-resolution. At the same time, a deeper insight into the effect of quasi-compressible LB schemes on pressure-dominated turbulence production is also called for, as shown by the disagreement of the current study in the extreme near-field of the SSG that is independent of collision model.

## CRedit authorship contribution statement

**Chin Vern Yeoh:** Conceptualization, Methodology, Software, Validation, Investigation, Formal analysis, Writing - original draft, Writing - review & editing, Visualization. **Ean Hin Ooi:** Conceptualization, Methodology, Supervision, Project administration. **Ji Jinn Foo:** Conceptualization, Methodology, Resources, Writing - review & editing, Visualization, Supervision, Project administration, Funding acquisition.

## Declaration of competing interest

The authors declare that they have no known competing financial interests or personal relationships that could have appeared to influence the work reported in this paper.

## Acknowledgements

The authors wish to thank Monash University Malaysia for providing the financial support under the Monash Malaysia Merit Scholarship Programme (MUM-25469878) that enabled the current research project. Specific acknowledgement is also given to the Monash University Malaysia High Performance Computing (MUM-HPC) platform for its provision of computational resources. Moreover, the authors wish to thank, in no particular order, Prof. Soh Ai Kah, A/Prof. Ng Khai Ching, Dr. Tan Ming Kwang, Mr. Teh An Liang, and Ms. Hoi Su Min for their thoughtful suggestions and discussions which improved various facets of the current study, ranging from the numerical fundamentals to turbulence results. Lastly, the authors express their gratitude to the reviewers of this manuscript, whose input and comments have served to improve the quality and readability of the current work.

## References

- [1] A.J.C. Ladd, Numerical simulations of particulate suspensions via a discretized Boltzmann-equation. Part 1. Theoretical foundation, *J. Fluid Mech.* 271 (1994) 285–309.
- [2] E.M. Viggen, Acoustic multipole sources for the lattice Boltzmann method, *Phys. Rev. E* 87 (2013).
- [3] Y.H. Yip, A.K. Soh, J.J. Foo, Flow-dynamics induced thermal management of crude oil wax melting: Lattice Boltzmann modeling, *Int. J. Therm. Sci.* 137 (2019) 675–691.
- [4] C.K. Aidun, J.R. Clausen, Lattice-Boltzmann method for complex flows, *Annu. Rev. Fluid Mech.* 42 (2010) 439–472.
- [5] P. Nathen, D. Gaudlitz, M.J. Krause, N.A. Adams, On the stability and accuracy of the BGK, MRT and RLB Boltzmann schemes for the simulation of turbulent flows, *Commun. Comput. Phys.* 23 (2018) 846–876.
- [6] G.R. McNamara, G. Zanetti, Use of the Boltzmann equation to simulate lattice-gas automata, *Phys. Rev. Lett.* 61 (1988) 2332.
- [7] Y. Qian, D. d’Humières, P. Lallemand, Lattice BGK models for Navier–Stokes equation, *EPL Europhys. Lett.* 17 (1992) 479.
- [8] D. d’Humières, Generalized lattice-Boltzmann equations, in: *Rarefied Gas Dynamics*, 1992.
- [9] M. Geier, A. Greiner, J.G. Korvink, Cascaded digital lattice Boltzmann automata for high Reynolds number flow, *Phys. Rev. E* 73 (2006).
- [10] M. Geier, M. Schönherr, A. Pasquali, M. Krafczyk, The cumulant lattice Boltzmann equation in three dimensions: Theory and validation, *Comput. Math. Appl.* 70 (2015) 507–547.
- [11] P. Lallemand, L.-S. Luo, Theory of the lattice Boltzmann method: Dispersion, dissipation, isotropy, Galilean invariance, and stability, *Phys. Rev. E* 61 (2000) 6546.
- [12] K. Timm, H. Kusumaatmaja, A. Kuzmin, *The Lattice Boltzmann Method: Principles and Practice*, Springer, Berlin, Germany, 2016.
- [13] K. Suga, Y. Kuwata, K. Takashima, R. Chikase, A D3Q27 multiple-relaxation-time lattice Boltzmann method for turbulent flows, *Comput. Math. Appl.* 69 (2015) 518–529.
- [14] I.V. Karlin, A. Ferrante, H.C. Öttinger, Perfect entropy functions of the lattice Boltzmann method, *EPL Europhys. Lett.* 47 (1999) 182.
- [15] S. Ansumali, I.V. Karlin, Stabilization of the lattice Boltzmann method by the H theorem: A numerical test, *Phys. Rev. E* 62 (2000) 7999.
- [16] F. Tosi, S. Ubertini, S. Succi, H. Chen, I.V. Karlin, Numerical stability of entropic versus positivity-enforcing lattice Boltzmann schemes, *Math. Comput. Simulation* 72 (2006) 227–231.
- [17] B.M. Boghosian, J. Yezep, P.V. Coveney, A. Wager, Entropic lattice Boltzmann methods, *Proc. R. Soc. Lond. Ser. A Math. Phys. Eng. Sci.* (2001) 717–766.
- [18] M. Spasov, D. Rempfer, P. Mokhasi, Simulation of a turbulent channel flow with an entropic lattice Boltzmann method, *Int. J. Numer. Methods Fluids* 60 (2009) 1241–1258.
- [19] C. Flint, G. Vahala, Partial entropic stabilization of lattice Boltzmann magnetohydrodynamics, *Phys. Rev. E* 97 (2018) 013302.
- [20] F. Tosi, S. Ubertini, S. Succi, I.V. Karlin, Optimization strategies for the entropic lattice Boltzmann method, *J. Sci. Comput.* 30 (2007) 369.
- [21] I.V. Karlin, F. Bösch, S. Chikatamarla, Gibbs’ principle for the lattice-kinetic theory of fluid dynamics, *Phys. Rev. E* 90 (2014) 031302.
- [22] F. Bösch, S.S. Chikatamarla, I.V. Karlin, Entropic multirelaxation lattice Boltzmann models for turbulent flows, *Phys. Rev. E* 92 (2015) 043309.
- [23] B. Dorschner, S.S. Chikatamarla, I.V. Karlin, Transitional flows with the entropic lattice Boltzmann method, *J. Fluid Mech.* 824 (2017) 388–412.
- [24] B. Dorschner, S.S. Chikatamarla, I.V. Karlin, Entropic multirelaxation-time lattice Boltzmann method for moving and deforming geometries in three dimensions, *Phys. Rev. E* 95 (2017).
- [25] B. Dorschner, S.S. Chikatamarla, I.V. Karlin, Fluid–structure interaction with the entropic lattice Boltzmann method, *Phys. Rev. E* 97 (2018).
- [26] O. Malaspinas, M. Deville, B. Chopard, Towards a physical interpretation of the entropic lattice Boltzmann method, *Phys. Rev. E* 78 (2008) 066705.
- [27] M. Gehrke, C. Janßen, T. Rung, Scrutinizing lattice Boltzmann methods for direct numerical simulations of turbulent channel flows, *Comput. Fluids* 156 (2017) 247–263.
- [28] R. Benzi, S. Succi, Two-dimensional turbulence with the lattice Boltzmann equation, *J. Phys. A: Math. Gen.* 23 (1990) L1.
- [29] D.O. Martinez, W.H. Matthaeus, S. Chen, D. Montgomery, Comparison of spectral method and lattice Boltzmann simulations of two-dimensional hydrodynamics, *Phys. Fluids* 6 (1994) 1285–1298.
- [30] C. Peng, N. Geneva, Z. Guo, L.-P. Wang, Direct numerical simulation of turbulent pipe flow using the lattice Boltzmann method, *J. Comput. Phys.* 357 (2018) 16–42.
- [31] J. Meyers, P. Sagaut, On the model coefficients for the standard and the variational multi-scale Smagorinsky model, *J. Fluid Mech.* 569 (2006) 287–319.
- [32] Y.-H. Dong, P. Sagaut, A study of time correlations in lattice Boltzmann-based large-eddy simulation of isotropic turbulence, *Phys. Fluids* 20 (2008) 035105.
- [33] G. Jin, S. Wang, Y. Wang, G. He, Lattice Boltzmann simulations of high-order statistics in isotropic turbulent flows, *Appl. Math. Mech.* 39 (2018) 21–30.
- [34] K.N. Premnath, M.J. Pattison, S. Banerjee, Computation of transitional flow past a circular cylinder using multiblock lattice Boltzmann method with a dynamic subgrid scale model, *Fluid Dyn. Res.* 45 (2013) 055510.
- [35] L. Djenidi, Lattice-Boltzmann simulation of grid-generated turbulence, *J. Fluid Mech.* 552 (2006) 13–35.

- [36] B. Keating, G. Vahala, J. Yepez, M. Soe, L. Vahala, Entropic lattice Boltzmann representations required to recover Navier–Stokes flows, *Phys. Rev. E* 75 (2007) 036712.
- [37] C. Feuchter, O. Wagner, A. Stief, T. Beisswenger, Turbulent flow simulations around a surface-mounted finite cylinder using an entropic multi-relaxation lattice Boltzmann method, *Fluid Dyn. Res.* 51 (2019) 055509.
- [38] W. Baines, E. Peterson, An investigation of flow through screens, *Trans. Am. Soc. Mech. Engrs.* 73 (1951).
- [39] P. Roach, The generation of nearly isotropic turbulence by means of grids, *Int. J. Heat Fluid Flow* 8 (1987) 82–92.
- [40] D. Hurst, J. Vassilicos, Scalings and decay of fractal-generated turbulence, *Phys. Fluids* 19 (2007) 035103.
- [41] N. Mazellier, J. Vassilicos, Turbulence without Richardson–Kolmogorov cascade, *Phys. Fluids* 22 (2010) 075101.
- [42] P. Valente, J.C. Vassilicos, The decay of turbulence generated by a class of multiscale grids, *J. Fluid Mech.* 687 (2011) 300–340.
- [43] G. Melina, P.J. Bruce, J. Vassilicos, Vortex shedding effects in grid-generated turbulence, *Phys. Rev. Fluids* 1 (2016) 044402.
- [44] G. Cafiero, G. Castrillo, C.S. Greco, T. Astarita, Effect of the grid geometry on the convective heat transfer of impinging jets, *Int. J. Heat Mass Transfer* 104 (2017) 39–50.
- [45] G. Melina, P. Bruce, J. Nedić, S. Tavoularis, J. Vassilicos, Heat transfer from a flat plate in inhomogeneous regions of grid-generated turbulence, *Int. J. Heat Mass Transfer* 123 (2018) 1068–1086.
- [46] G. Melina, P. Bruce, G. Hewitt, J. Vassilicos, Heat transfer in production and decay regions of grid-generated turbulence, *Int. J. Heat Mass Transfer* 109 (2017) 537–554.
- [47] S.M. Hoi, A.L. Teh, E.H. Ooi, I.M.L. Chew, J.J. Foo, Forced convective heat transfer optimization of plate-fin heat sink with insert-induced turbulence, *Appl. Therm. Eng.* 160 (2019) 114066.
- [48] Y. Zhou, K. Nagata, Y. Sakai, H. Suzuki, Y. Ito, O. Terashima, et al., Relevance of turbulence behind the single square grid to turbulence generated by regular-and multiscale-grids, *Phys. Fluids* 26 (2014) 075105.
- [49] Y. Zhou, K. Nagata, Y. Sakai, H. Suzuki, Y. Ito, O. Terashima, Development of turbulence behind the single square grid, *Phys. Fluids* 26 (2014) 045102.
- [50] Y. Zhou, K. Nagata, Y. Sakai, Y. Ito, T. Hayase, Enstrophy production and dissipation in developing grid-generated turbulence, *Phys. Fluids* 28 (2016) 11.
- [51] S. Laizet, J. Nedić, C. Vassilicos, Influence of the spatial resolution on fine-scale features in DNS of turbulence generated by a single square grid, *Int. J. Comput. Fluid Dyn.* 29 (2015) 286–302.
- [52] I. Paul, G. Papadakis, J. Vassilicos, Genesis and evolution of velocity gradients in near-field spatially developing turbulence, *J. Fluid Mech.* 815 (2017) 295–332.
- [53] T. Watanabe, Y. Sakai, K. Nagata, Y. Ito, T. Hayase, Implicit large eddy simulation of a scalar mixing layer in fractal grid turbulence, *Phys. Scr.* 91 (2016) 074007.
- [54] I. Paul, G. Papadakis, J. Vassilicos, Direct numerical simulation of heat transfer from a cylinder immersed in the production and decay regions of grid-element turbulence, *J. Fluid Mech.* 847 (2018) 452–488.
- [55] S.K. Kang, Y.A. Hassan, The effect of lattice models within the lattice Boltzmann method in the simulation of wall-bounded turbulent flows, *J. Comput. Phys.* 232 (2013) 100–117.
- [56] X. Shan, H. Chen, Lattice Boltzmann model for simulating flows with multiple phases and components, *Phys. Rev. E* 47 (1993) 1815.
- [57] A. Kupershtokh, D. Medvedev, D. Karpov, On equations of state in a lattice Boltzmann method, *Comput. Math. Appl.* 58 (2009) 965–974.
- [58] J. Smagorinsky, General circulation experiments with the primitive equations: I. The basic experiment, *Mon. Weather Rev.* 91 (1963) 99–164.
- [59] S. Hou, J. Sterling, S. Chen, G. Doolen, A lattice Boltzmann subgrid model for high Reynolds number flows, 1994, arXiv preprint [arXiv:comp-gas/9401004](https://arxiv.org/abs/9401004).
- [60] R. Gomes-Fernandes, B. Ganapathisubramani, J. Vassilicos, Particle image velocimetry study of fractal-generated turbulence, *J. Fluid Mech.* 711 (2012) 306–336.
- [61] K. Nagata, T. Saiki, Y. Sakai, Y. Ito, K. Iwano, Effects of grid geometry on non-equilibrium dissipation in grid turbulence, *Phys. Fluids* 29 (2017) 015102.
- [62] S. Izquierdo, N. Fueyo, Characteristic nonreflecting boundary conditions for open boundaries in lattice Boltzmann methods, *Phys. Rev. E* 78 (2008) 046707.
- [63] P. Lammers, K. Beronov, R. Volkert, G. Brenner, F. Durst, Lattice BGK direct numerical simulation of fully developed turbulence in incompressible plane channel flow, *Comput. Fluids* 35 (2006) 1137–1153.
- [64] G.K. Batchelor, A.A. Townsend, Decay of turbulence in the final period, *Proc. R. Soc. Lond. Ser. A Math. Phys. Eng. Sci.* 194 (1948) 527–543.
- [65] P. Davidson, *Turbulence: An Introduction for Scientists and Engineers*, Oxford University Press, USA, 2015.
- [66] H. Tennekes, J.L. Lumley, *A First Course in Turbulence*, MIT Press, 1972.
- [67] A. Tsinober, *An Informal Conceptual Introduction to Turbulence*, Vol. 483, Springer, 2009.
- [68] M. Junk, A. Klar, L.-S. Luo, Asymptotic analysis of the lattice Boltzmann equation, *J. Comput. Phys.* 210 (2005) 676–704.
- [69] K. Dullenkopf, R. Mayle, E. Darryl, Metzger memorial session paper: An account of free-stream-turbulence length scale on laminar heat transfer, *J. Turbomach.* 117 (1995) 401–406.